Research Paper

A numerical simulation approach to the crater-scaling relationships in low-speed impacts under microgravity

Onur Çelik [a],[*],[1], Ronald-Louis Ballouz [b],[2], Daniel J. Scheeres [c], Yasuhiro Kawakatsu [d]

[a] *University of Glasgow, G12 8QQ, Glasgow, Scotland, United Kingdom*
[b] *Lunar and Planetary Lab., University of Arizona, Tucson, AZ 85721, United States*
[c] *University of Colorado Boulder, CO 80309, United States*
[d] *Japan Aerospace Exploration Agency (JAXA), Sagamihara, 252-5210, Japan*

ARTICLE INFO

ABSTRACT

The many small-body exploration missions that have occurred over the last few decades have shown that small solar system objects are covered with granular material of varying depth. These missions have also observed that granular materials are mobilized from the surfaces at speeds on the order of escape speed by different contributing mechanisms. Those result in various outcomes including escape and reimpact. The latter contributes to further impact-driven evolution. Despite the long history of the research in the field of planetary cratering, low-speed impacts have not been studied extensively under gravity levels relevant to small-bodies. Earth-based low-gravity platforms lack the ability to probe microgravity impact physics for a sufficiently long duration to collect meaningful data from experiments. In order to overcome these challenges, this study uses discrete-element method (DEM) simulations to test low-speed cratering at 5–50 cm/s in granular materials in microgravity. The study first presents a procedure for post-processing the raw simulation data to extract the information relevant to the crater-scaling relationships and demonstrates their applicability for crater sizes, ejecta properties and crater formation time. The implications of the results are discussed in the light of results from recent small-body exploration missions.

1. Introduction

Remote-sensing observations and ground-truth from the asteroid and comet rendezvous missions NEAR-Shoemaker, Hayabusa, Rosetta, Hayabusa2 as well as the flybys during Galileo, Stardust (also Rosetta and NEAR-Shoemaker) missions have all shown that small solar system objects (hereafter small-bodies) are covered with granular material at varying depth and particle sizes and numerous craters of different sizes (Sullivan et al., 2002; Miyamoto et al., 2007; Mottola et al., 2015; Brownlee et al., 2004). Recent small-body exploration missions OSIRIS-REx and Hayabusa2 have also demonstrated that asteroids are more active than previously anticipated. As shown during the OSIRIS-REx mission, asteroid Bennu ejects material from its surface (up to centimeter in size) through multiple potentially contributing mechanisms (Lauretta et al., 2019; Chesley et al., 2020; Bottke et al., 2020). Most of the ejected materials fall back on the surface at speeds much less than a meter per second, after a brief orbital motion (Geissler

et al., 1996; Hergenrother et al., 2020), possibly denting the surface and forming craters at lower speeds, though none have been observed. Similarly, it was speculated that the dimples in the plains of Itokawa may have been formed by low-speed impacts, albeit likely by larger impactors than those observed in Bennu (Kiuchi et al., 2019). This suggests that there is an incessant evolution across small-body surfaces through impacts, and not necessarily triggered by singular large-scale events, but enabled by smaller ones, as well. Understanding the formation of those craters would shed light on their evolution in more detail, and provide a better understanding of the possibility of secondary cratering in a micro-gravity environment (Walsh et al., 2019). Moreover, with increasing interest on ground-truth measurements, exploration missions have prioritized (near-)surface operations via hovering, sampling, deploying small landers, and performing impact experiments (Tsuda et al., 2020). In particular, surface sampling by larger spacecraft and the bouncing motion of small landers would cause

---

similar low-speed impact craters in the low-gravity environment of small bodies, such as in the case of the Philae lander of the Rosetta mission or OSIRIS-REx Touch-and-Go sampling (Biele et al., 2015; Lauretta and OSIRIS-REx TAG Team, 2021). Understanding these low-speed impact events through quantifying their sizes and ejection properties would not only allow an interpretation of the surface mechanical properties but also allow more informed space mission operations in these hostile environments (Çelik et al., 2019; Thuillet et al., 2020; Murdoch et al., 2021).

However, the quantitative understanding of craters on planetary bodies has largely been focused on highly energetic impacts, due to their catastrophic results and role they have played in the evolution of solar system bodies. Also the lack of observations of small bodies until recently has led to a dearth of data in this regime. Cratering at high-energy impacts involve complex processes, including thermodynamic phase changes in materials and break-ups (Melosh, 1989), whose sophisticated numerical simulations require high computational power. Early studies therefore focused on impact experiments with granular and other type of materials and developed the π-scaling relationships in order to find mathematical relationships between the properties of craters and the macro properties of a target and an impactor (Gault and Wedekind, 1977; Schmidt, 1980; Holsapple and Schmidt, 1982; Housen et al., 1983; Schmidt and Housen, 1987). The resulting scaling relationships connected properties such as gravity, impactor and target density to crater sizes and ejected material velocity and its mass. Subsequent efforts have been focused on constraining its scaling coefficients for different materials and exploring the limits of its applicability (Housen and Holsapple, 2011).

Crater-scaling studies have more recently been extended to lower speed impacts in granular materials. For instance, Yamamoto et al. (2006) investigated transient crater growth in impacts at speeds between 11 and 329 m/s and provided measurements on crater sizes and depths (Yamamoto et al., 2006). Tsujido et al. (2015) studied ejecta velocity distribution in ~200 meter-per-second impacts varying the density of impactors in order to test the impactor-density dependency on crater scaling relationships (Tsujido et al., 2015). For lower speed impacts, Takizawa and Katsuragi (2020) expanded the work of Hayashi and Sumita (2017) and performed impact experiments at 1–97 m/s in granular slopes, where the authors expanded the existing crater scaling relationships to also account for the effects of impacts onto inclined planes, and suggested the universality of the relationships (Takizawa and Katsuragi, 2020). Even though it is not in the planetary cratering context discussed here, De Vet and De Bruyn (2007) demonstrated the impact-energy dependency of crater sizes in very low speed impacts at 0.6–4.4 m/s (De Vet and De Bruyn, 2007).

There have also been recent efforts to test the limits of applicability of scaling relationships for low-gravity applications. Kiuchi et al. (2019) tested the effect of atmospheric pressure for impacts at 1–4.6 m/s under the gravity levels between that of the Moon and the Earth. The authors suggested that the scaling relationships could be applied to several meter-per-second impact speeds (Kiuchi et al., 2019). In a higher speed but lower gravity level case, Thuillet et al. (2020) investigated the crater formation and ejecta characteristics with discrete-element method simulations of 50–300 m/s impacts in the context of spacecraft sampling in asteroids (Thuillet et al., 2020). In a recent study, Wright et al. (2020) performed low-speed oblique impact experiments to understand the ricochet and cratering processes in more detail, with applications to recently observed activity on the asteroid Bennu.

The fundamental difference between low- and the high-speed impacts is that there are no drastic thermodynamic changes during or after an impact in the former. The target material would merely be ejected, or pushed in different directions, as the impactor penetrates down or bounces off a granular bed, with the rigid-body assumption remaining valid. For impacts with speeds on the order of a few meter-per-second,

the crater formation takes less than a second under the Earth conditions, within which no significant material ejection occurs. Yet, it appears that similar crater scaling relationships may apply to those impacts as well (Takizawa and Katsuragi, 2020). However, testing those scaling relationships at extremely low-speed impacts, e.g. below meter-per-second, in low-gravity environments is not as straightforward, even though they are likely to constitute the most frequent impact events. As the recent SCI experiment during the Hayabusa2 mission demonstrated, cratering time evolution under low gravity is much longer (more than 5 min in the SCI case) than those experienced on the Earth, even in kilometer-per-second impact speeds (Arakawa et al., 2020). This was also observed during the first impact of Philae lander on comet 67P which impacted the surface at ~1 m/s (Biele et al., 2015). Moreover, both natural and humanmade objects are found to ricochet or bounce off the surface upon low-energy impacts in microgravity environments (Biele et al., 2015; Lauretta et al., 2019; Scholten et al., 2019; Chesley et al., 2020). Impact experiments with sub-meter-per-second impacts would not yield significant insights under Earth conditions, even if the measurement challenges of the rapid crater formation is overcome. On the other hand, the Earth-based low-gravity platforms, such as drop towers, parabolic flights and the International Space Station (ISS) and other lab-based platforms, which typically only provide seconds-to-minutes of a simulated low-gravity environment, lack the level and duration of low gravity, or the access to and controllability in experiments, as well as the sufficient quantitative measurements. Even if some of these problems may be overcome with alternative platforms, such as air-bearing platforms (Van wal et al., 2021) or inclined granular planes (Takizawa and Katsuragi, 2020), handling the granular materials in those platforms for reliable measurements is extremely challenging. To that end, there are only a handful of experiments which successfully perform impacts on a granular bed under relatively long duration low-gravity in parabolic and space shuttle flights (Cintala et al., 1989; Colwell and Taylor, 1999; Colwell et al., 2008; Brisset et al., 2018), and with an exception of Cintala et al. (1989) for km/s-speed impacts, they have mostly yielded limited quantitative insights into cratering. Considering the extremely limited access to the ISS, it appears that it is practically not feasible to perform impact experiments to test the applicability of the crater-scaling relationships in the low-speed, low-gravity impact regime.

In order to overcome these limitations, discrete-element method (DEM) simulations are used to simulate the impact regimes that would be encountered in small-body environments (Sánchez and Scheeres, 2011). The DEM simulations can avoid the limited low-gravity time and test condition restrictions, as well as vibration-caused noisy data in drop towers and parabolic flights while allowing to perform "experiments" in virtually any gravitational environment. As the state of each particle is recorded, the computational nature of DEM simulations provide a quantitative framework that enables particle-level analysis to test the subject of interest. Thus far, DEM simulations have been applied in a variety of studies pertinent to small-body and low-gravity applications, including but not limited to, landing, sampling and general granular mechanics studies (Schwartz et al., 2014; Maurel et al., 2018; Thuillet et al., 2018; Cheng et al., 2019; Çelik et al., 2019). In the cratering context, DEM simulations, the obtained post-processed data would not only provide insights into crater size and depth, as typically available in the experimental literature, but also ejection properties, i.e. amount, velocity, angle, as well as formation time, which are either not available or available only in a limited way.

In this paper, the applicability of the crater-scaling relationships is investigated for gravity-regime craters in low-speed impacts under low gravity with the goal to justify the opportunities provided by the DEM simulations. The study first investigates the experimental and space mission data for crater sizes (as the most commonly investigated result) and presents a case on the potential applicability of the crater-scaling relationships for the interested impact regime. Building upon this, a set of DEM simulations are presented and analyzed. The study employs a

parallelized state-of-the-art DEM code `pkdgrav`, which treats particle collisions with a soft-sphere DEM (SSDEM) method (Schwartz et al., 2012). Impact speeds between 5 cm/s and 50 cm/s are considered at the microgravity gravity level. The speed range is selected from the most frequent ejection speeds on Bennu and OSIRIS-REx touchdown speed on Bennu's surface (Pelgrift et al., 2020; Lauretta and OSIRIS-REx TAG Team, 2021). A systematic computational approach is proposed to post-process the raw DEM simulation data in order to extract not only crater sizes and depths, but also the velocity, angle and the amount of ejected material and crater formation time. The processed data is analyzed individually and in comparison with the existing lab-based and space-mission data to test the crater-scaling relationships at the studied impact regime, especially in the cases where the impactor bounces instead of submerging. The implications of the found results are also discussed in the light of recent small-body exploration missions.

The paper is structured as follows: In Section 2, the crater-scaling relationships are summarized. In Section 3, the existing literature and a case for the potential applicability of the scaling relationships are presented. In Section 4, the details of the DEM simulations and the proposed post-processing approach are introduced. In Section 5, the results of the post-processed are presented and discussed together with the scaling relationship results, before presenting conclusions in Section 6.

2. The crater-scaling relationships

2.1. Scaling of crater sizes

Scaling relationships were first investigated for large planetary craters because telescopic observations permit only large ones to be observed. Large planetary craters are typically formed at extremely high speeds, usually on the order of kilometer-per-second or more. In this regime of formation, the process is extremely complex: Impactors break apart, melt, vaporize, mix with surface material and materials are ejected from the crater cavity or pushed down deeper (Melosh, 1989). In the absence of large computational simulations, the pioneers focused on analytical models derived from empirical studies with buried explosives or high-speed impacts. Dimensional analysis with π-theorem (Buckingham, 1914) was proposed to characterize crater and ejecta properties in the form of power-law scaling, and as a function of impact, impactor and macro surface properties (i.e. gravity, strength, density), avoiding granular level complexity (Holsapple and Schmidt, 1982; Housen et al., 1983; Schmidt, 1980; Schmidt and Housen, 1987; Holsapple, 1993). The fundamental relationships presented in various studies in Holsapple and Schmidt (1982), Housen et al. (1983), Schmidt (1980), Schmidt and Housen (1987), Melosh (1989), Holsapple (1993) and Housen and Holsapple (2011) are summarized hereafter.

The assumption of the theory is that a few key parameters can be utilized in a functional relationship, such as in crater volume below:

$$V = f(a, \delta, U, \rho, Y, g) \qquad (1)$$

Eq. (1) includes a total of 7 parameters (including crater volume, V), which are described in the units of mass, length and time. Those parameters will be referenced frequently in the later parts of this paper, hence it is given in Table 1 with their definitions.

According to Π-theorem, those 7 parameters can be reduced to 7 - 3 = 4 dimensionless parameters as shown in Eq. (2):

$$\pi_V = V \frac{\rho}{m} \qquad (2a)$$

$$\pi_2 = \frac{ga}{U^2} \qquad (2b)$$

$$\pi_3 = \frac{Y}{\rho U^2} \qquad (2c)$$

$$\pi_4 = \frac{\rho}{\delta} \qquad (2d)$$

Table 1
Glossary of crater-scaling relationships.

Symbol	Definition
V	Crater volume [m³]
a	Impactor radius [m]
δ	Impactor density [kg/m³]
U	Impact velocity [m/s]
ρ	Target bulk density [kg/m³]
Y	Target strength [Pa]
g	Gravity [m/s²]

In Eq. (2), π_V is defined as "normalized volume". π_2 is so called "gravity-scaling parameter", and a measure of gravity in the crater size and equals the inverse Froude number. It is also written as $\pi_2 = g/U^2(m/\delta)^{1/3} = 3.22ga/U^2$ (Schmidt, 1980), but the constant is generally omitted.

The third equation π_3 is "nondimensional strength" and indicates the strength contribution in the cratering. Note that strength effect is not considered in the research and it is only provided for the sake of completeness here. Finally, π_4 is target-to-impactor density ratio. Combining equations in (2) in order to create a functional relation as in Eq. (1) yield

$$\pi_V = K_V \pi_2^{-\alpha} \pi_3^{-\beta} \pi_4^{-\gamma} \qquad (3)$$

where K_V, α, β, γ are constants that are generally determined experimentally (Holsapple, 1993). Schmidt and Housen (1987) makes use of a coupling parameter $C = aU^\mu \delta^\nu$ and rewrite Eq. (1) as

$$V = f(C, \rho, Y, g) \qquad (4)$$

Note that the introduction of C means that "late-stage equivalence" of cratering (Schmidt and Housen, 1987) is assumed to apply to the impact regime in this paper. This assumption is not yet clear for such low-speed impacts under microgravity, but the demonstrated applicability of the scaling relationships in predicting the outcomes of low-speed impacts (Kiuchi et al., 2019; Takizawa and Katsuragi, 2020) suggests that it may be valid. With dimensional analysis applied again to Eq. (4), the crater volume expression takes the following form:

$$V = K_1 \left\{ \pi_2 \pi_4^{\frac{6\nu-2-\mu}{3\mu}} + \left[K_2 \pi_3 \pi_4^{\frac{6\nu-2}{3\mu}} \right]^{\frac{2+\mu}{2}} \right\}^{\frac{-\mu}{2+\mu}} \qquad (5)$$

The μ exponent expresses a mode of coupling between the impactor and the target (Housen et al., 1983). It lies between $1/3 \leq \mu \leq 2/3$, in which the lower and higher ends of that range signifies impactor momentum or impactor energy, respectively, as the main driver of the crater size (Housen et al., 1983). ν, on the other hand, is an exponent relating the target and impactor densities. Housen and Holsapple (2011) states that ν is well-constrained to 0.4, *i.e.*, cratering efficiency is independent of target or impactor density. However, in a study conducted by Tsujido et al. (2015), higher values ($\sim$0.57) were also found (Tsujido et al., 2015).

If the K_2 term in Eq. (5) is assumed to be close to 1, an "effective" strength can be defined as $\bar{Y} = K_2 Y$ (Holsapple, 1993). Substituting the π values in Eq. (2) into Eq. (5) yield

$$\pi_V = K_1 \left(\frac{m}{\rho}\right) \left\{ \left(\frac{ga}{U^2}\right)\left(\frac{\rho}{\delta}\right)^{\frac{6\nu-2-\mu}{3\mu}} + \left[\left(\frac{\bar{Y}}{\rho U^2}\right)\left(\frac{\rho}{\delta}\right)^{\frac{6\nu-2}{3\mu}} \right]^{\frac{2+\mu}{2}} \right\}^{\frac{-\mu}{2+\mu}} \qquad (6)$$

In Eq. (6), K_1, μ, ν and $\bar{Y}$ are material-dependent and experimentally-determined constants (Holsapple, 1993). Although the expression is given for crater volume, it is often easier to observe or measure crater radius or diameter. If a crater is simplified as a paraboloid (Melosh, 1989), then its volume can be written in terms crater dimensions as

$$V = \frac{1}{2} \pi R_a R_b d \qquad (7)$$

where d is crater depth and, R_a and R_b are major and minor axis dimensions of an ellipsoidal paraboloid, often taken as a mean radius,

hence $R_a = R_b$. In craters formed by kilometer-per-second magnitude impacts, d is found to be between $R/2$ and $2R/3$ (Schmidt and Housen, 1987; Melosh, 1989). If one makes the assumption $R \sim V^{1/3}$ to rewrite Eq. (6) in terms of crater radius, it yields:

$$R = K_R\left(\frac{m}{\rho}\right)^{\frac{1}{3}} \left\{ \left(\frac{ga}{U^2}\right)\left(\frac{\rho}{\delta}\right)^{\frac{6v-2-\mu}{3\mu}} + \left[\left(\frac{\bar{Y}}{\rho U^2}\right)\left(\frac{\rho}{\delta}\right)^{\frac{6v-2}{3\mu}}\right]^{\frac{2+\mu}{2}} \right\}^{\frac{-\mu}{2+\mu}} \quad (8)$$

which defines cratering efficiency in terms of crater radius as

$$\pi_R = R\left(\frac{\rho}{m}\right)^{1/3} \quad (9)$$

Now that the equations are presented, it is possible to discuss the regimes of the cratering process, defined in different works (Holsapple and Schmidt, 1982; Housen et al., 1983). In general, if the first term inside the curly bracket in Eqs. (6) and (8) is much greater than the second, then a cratering process is stated to be "gravity-dominated" and the second term in the parenthesis in Eqs. (6) and (8) can be ignored. The craters on dry granular materials on the Earth are almost always gravity-dominated, because the effective strength in dry granular material is caused by the angle of friction between grains and not as part of the material structure (Housen and Holsapple, 2011). Cohesive strength, on the other hand, is too small to overcome this in most cases. However, it is worth noting that in low-gravity environments, strength arising from cohesive forces between grains may, in fact, be as important as its gravitational counterpart, hence one can observe craters occurring in strength regime (Scheeres et al., 2010). It has been speculated that the Deep impact crater on comet Tempel-1 may, in fact, have been formed in strength regime (Richardson et al., 2007). However, since the current manuscript only deals with craters formed in the gravity regime, the remainder of the paper will only focus on gravity-dominated craters.

2.2. Scaling of ejection properties

Similar to size-scaling of craters, ejection velocity and ejected mass can also be expressed with a group of power-law scaling relationships (Housen et al., 1983). Ejection velocity can be described as a function of crater properties as below (Housen and Holsapple, 2011):

$$v(r) = C_1 \sqrt{gR}\left(\frac{r}{R}\right)^{-1/\mu} \quad (10)$$

where r denotes the radial launch position of material from the impact point and C_1 is the coefficient found after fitting the data. The other terms are same as those used in the crater size scaling in previous subsection.

Another aspect of the crater-scaling relationships is "mass ejected faster than velocity v", M. In other words, it refers to cumulative or total mass of particles whose velocity higher than some given velocity v. Because of intrinsic position dependence of v, ejected mass is largely representative of mass as a function of distance from the launch point, even though it is not directly a function of r. $M(v)$ can then be expressed as (Housen and Holsapple, 2011):

$$M(v) = C_2 \rho R^3 \left(\frac{v}{\sqrt{gR}}\right)^{-3\mu} \quad (11)$$

C_2 also denotes an experimentally-determined coefficient. Note that both Eq. (10) and (11) are written in terms of crater size. Equivalent expressions can also be written in terms of impactor properties, which can be found in Housen and Holsapple (2011).

In a review provided in Housen and Holsapple (2011), the authors discuss the applicability range of ejecta-scaling relationships, its dependency to impact, impactor and surface parameters in the light of the experimental data to date, whose impact speed is greater than ~200 m/s (Housen and Holsapple, 2011). According to that study, the applicability range of the crater-scaling relationships is from some close distance from the impact point to near the crater rim for the power-law scaling. Near impactor, there would be no ejecta, or ejecta would

be in the form of a jetted mass, hence the scaling relationships are stated to not apply. On the other hand, near crater rim gravity/strength effects are more prominent, therefore the scaling also fails. According to Housen and Holsapple (2011), the range of applicability is within some $n_1 a \leq r \leq n_2 R$ where $n_1 \approx 1.2$ and $n_2 \approx 1$ (see Fig. 1).

The group of power-law scaling relationships presented can traditionally be illustrated with figures for ejection properties similar to Fig. 2, as adapted from Housen and Holsapple (2011).

Finally, crater formation time, T_g, has also been investigated within the crater-scaling studies. T_g captures the time from the beginning of impact and at the end of the excavation stage. It is among the hardest to measure parameters in empirical studies under Earth gravity due to rapid excavation, hence the despite large number of empirical studies on cratering, only a handful of them contain this information (Schmidt and Housen, 1987; Cintala et al., 1989). For craters in the gravity regime, T_g is given by Schmidt and Housen (1987) as:

$$T_g = K_{cr}\sqrt{\frac{V^{1/3}}{g}} = K_{cr}\sqrt{\frac{R}{g}} \quad (12)$$

where K_{cr} is the experimentally-derived coefficient that relates crater sizes to formation time. The K_{cr} is determined to be 1.6 by Melosh (1989) derived from Schmidt and Housen (1987), in which the value is presented as 0.8. However, it should be noted that the timescale of craters under Earth- and low-gravity could be very different. As an example, material ejection is observed ~400 s after the SCI impact (Arakawa et al., 2020). In the case of low-speed impacts in low gravity, long formation times may be expected, therefore a modification to K_{cr} value may be necessary, which will be discussed later.

3. The crater-size scaling in the literature

There has been a substantial effort to test the various aspects of crater-scaling relationships. The easiest measurable property of a crater is its size, therefore there is an abundance of data available in the literature for experiments at different speeds of impacts from m/s to km/s. In this section, a literature review is presented from a set of experiments at different impact conditions, and the scaling relationships with those will be investigated from the crater-size perspective to build a case for possible applicability of crater-scaling relationships in low-gravity and low-speed impact conditions. The list is not exhaustive and some very early or very recent studies may have been inadvertently omitted, but the list is expansive in its velocity range, which is between 1 m/s to 10 km/s. Table 2 summarizes the literature used.

Among the earlier studies, Gault and Wedekind (1977) and Cintala et al. (1989) investigated craters in lower gravity levels. The former study created the artificial low-gravity in a laboratory environment and performed a number of shots at 6.64 km/s. The latter utilized parabolic flights and performed impacts at one to two orders of magnitude lower velocities. Both studies only provided measurements of crater sizes relevant to this study.

Among the works specifically focusing on the high-speed craters, Cintala et al. (1999) crater sizes and ejection speeds in 7 recorded shots with speeds ranging between 0.8 and 1.9 km/s by high-speed imaging. Tsujido et al. (2015) investigated the effect of projectile density on the crater sizes and grain ejection velocities. Their impact velocities were between 105 and 215 m/s, i.e. an order of magnitude lower than those of the earlier studies (Housen and Holsapple, 2011; Gault and Wedekind, 1977; Schmidt, 1980). Yamamoto et al. (2006) investigated transient crater growth via impact experiments at speeds as low as 11 m/s (Yamamoto et al., 2006). The "low" velocity is a relative term here, as the highest impact velocity Yamamoto et al. (2006) is 329 m/s—higher than the highest velocity at Tsujido et al. (2015). More recently, Takizawa and Katsuragi (2020) tested cratering on inclined granular surfaces with meter-per-second level impact velocities (Takizawa and Katsuragi, 2020). The study has only a single data point at 1 m/s with lowest value after this being ~7 m/s (also
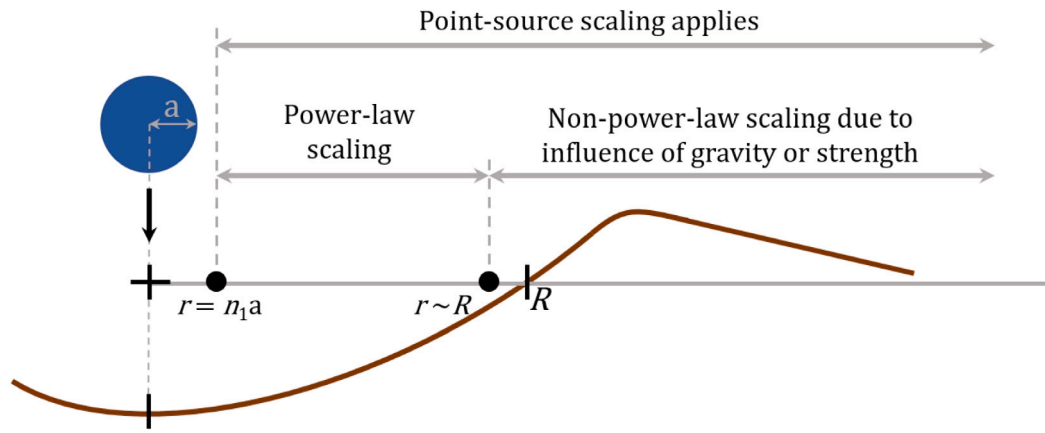
Fig. 1. Applicability range of power-law scaling.
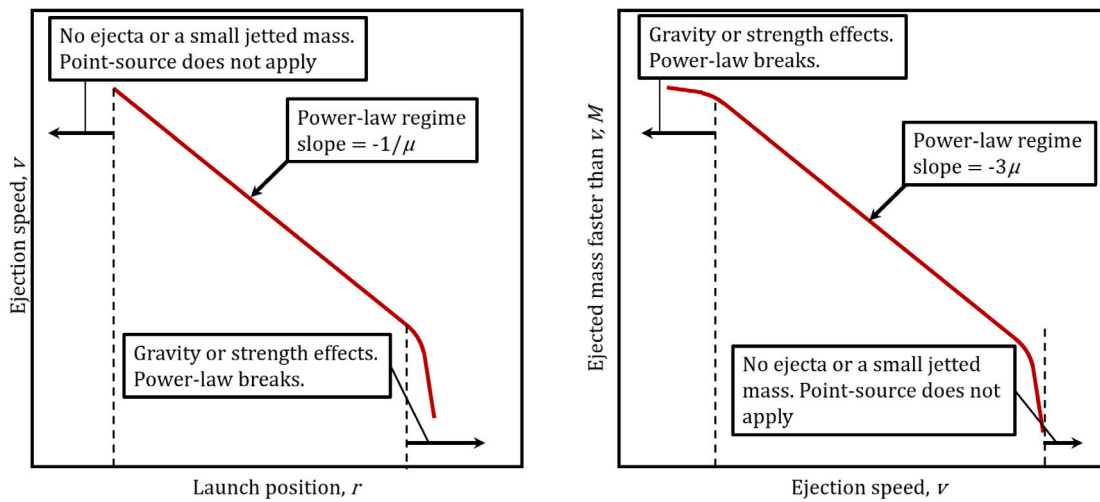*Source:* Adapted from Housen and Holsapple (2011).

Fig. 2. Power-law scaling of crater and ejecta.
Source: Adapted from Housen and Holsapple (2011).

Table 2
A list of previous studies on cratering. Acronyms: L—Laboratory, SC—Spacecraft.

#	Name	Type	Gravity [Earth-g]	Velocity range [m/s]	Measurement
1	Gault and Wedekind (1977)	L	0.073–1	6640	Crater size
2	Schmidt (1980)	L	1	1750–6410	Crater size
3	Cintala et al. (1989)	L	0.16–0.5	65–130	Crater size
4	Cintala et al. (1999)	L	1	800–1920	Crater size, ejection speed
5	Boudet et al. (2006)	L	1	2.65	Crater size, ejection speed
6	Yamamoto et al. (2006)	L	1	11–329	Crater size
7	Deboeuf et al. (2009)	L	1	1–4	Crater size, ejection speed
8	Housen and Holsapple (2011)	L	1	240–6670	Crater size, ejection speed, ejected mass
9	Tsujido et al. (2015)	L	1	106–215	Crater size
10	Takizawa and Katsuragi (2020)	L	1	1–97	Crater size
11	Richardson et al. (2007) and Richardson and Melosh (2013) (Deep Impact)	SC	3.46e−5	10 200	Crater size, ejection speed, ejected mass
12	Biele et al. (2015) (Philae)	SC	1.63e−5	1	Crater size
13	Arakawa et al. (2020) (Hayabusa2 - SCI)	SC	1.25e−5	2000	Crater size

single data point) and ~15 m/s (Takizawa and Katsuragi, 2020). The authors have also elucidated the cratering process at lower speeds while also developing improved crater-scaling relationships by incorporating impact angle and slope angle of the surface (Takizawa and Katsuragi, 2020). Because both studies tested cratering in inclined surfaces, the effective surface acceleration in local vertical is lower than the Earth's gravity.

The other low-gravity impact experiment examples are spacecraft craters. The Small Carry-On Impactor (SCI) experiment during the Hayabusa2 mission (2019) asteroid Ryugu and the impact of Deep Impact spacecraft (in 2005) comet Tempel-1 were performed at ~2 and ~10 km/s, respectively (Arakawa et al., 2020; Richardson et al., 2007). The SCI experiment is thus far the most controlled non-terrestrial impact experiment to date, from which crater size is calculated thanks to Hayabusa2 and DCAM3 images (Sawada et al., 2017; Arakawa et al., 2020). Possibly the most relevant to the study here, Rosetta mission's Philae lander impacted on comet 67P Churyumov/Gerasimenko occurred at ~1 m/s (Biele et al., 2015). Philae's first impact left a clear craters on the surface, which was later observed by the Rosetta spacecraft (Biele et al., 2015).

In addition to dedicated planetary cratering literature, there are also studies that focus on granular media and grain ejection dynamics in general. Among those, Deboeuf et al. (2009) derived an analytical model for dynamics of grain ejection from the impact experiments at 1–4 m/s (Deboeuf et al., 2009). Boudet et al. (2006) investigated the cratering dynamics in shallow sand layers in low-speed impacts (Boudet et al., 2006). The impact speeds were on the order of 2–3 m/s (Boudet et al., 2006), therefore relevant to this study. For both Boudet et al. (2006) and Deboeuf et al. (2009), crater radius can only be extracted from a single experimental run.

One can see in Table 2 that impact velocities are varied; the difference between the highest and the lowest is four orders of magnitude. This variation allows to test crater-scaling relationships at various impact velocities. Recall that all studies reported in Table 2 include crater size data in common, directly or indirectly. Therefore, the crater size-scaling relations in Eq. (8) is tested and the results are provided in Fig. 3.

Note that, the data in #10 includes highly-elliptical craters due to the oblique impacts, hence include two scales for an impact crater, major and minor axis radius. In that case, their average is used. Also note that neither Boudet et al. (2006) nor Deboeuf et al. (2009) measured or provided dedicated crater sizes in their studies, therefore crater radii (in both studies) were inferred indirectly from the given data in the respective studies. The reference line denoting $\pi_R = K_R \pi_2^{\frac{-\mu}{2+\mu}}$ was drawn with the impact, impactor and target properties used in Takizawa and Katsuragi (2020) and with generic parameters $K_R = 1.03$ and $\mu = 0.41$ from Holsapple and Housen (2007). The x-axis of Fig. 3 is π_2 or gravity-scaling parameter and y-axis is normalized crater radius, derived from Eq. (2). According to Fig. 3, there is a relatively strong correlation in the experimental results in terms of π-scaling. The crater-size data appear to be in agreement across different impact regimes. Especially the agreement of two low-gravity data at two different impact velocities (Gault and Wedekind, 1977; Cintala et al., 1989) suggests that the cratering scaling relationships may not only be valid under Earth-gravity but also valid under low-gravity. The recent SCI experiment on Ryugu further reinforces this statement. The agreement of these result with even lower velocity impacts under Earth gravity, is a further indication that the crater scaling relationships may be valid for low-speed impacts as well. This suggests a compelling evidence that the crater-scaling relationships may be valid for low-speed impacts under low-gravity, at least for the gravity-regime craters. Therefore, in order to test the hypothesis built here, and overcome the practical challenges to test the crater-scaling relationships under low-gravity, the discrete element method (DEM) simulations will be utilized.

4. Discrete-element method impact simulations under low-gravity conditions

A complete study of crater-scaling relationships, including crater size, ejection properties and formation time, of low-speed impacts under low-gravity conditions is currently missing in the literature. Collecting data from impacts at lower than meter-per-second is considerably difficult on the Earth due to the rapid formation of craters due to high gravitational acceleration. Similar but opposite measurement challenges exist in low-gravity platforms, such as parabolic flights or drop towers, in which limited low-gravity time prevents the observation of slow-forming craters. A long duration impact experiment campaign at the International Space Station (ISS) could provide suitable, albeit still challenging, conditions, to overcome measurement limitations under low gravity; however, the accessibility of the ISS is extremely limited. To overcome these limitations and bridge the aforementioned gap in literature, this study instead makes use of granular mechanics simulations with discrete-element method (DEM) in order to test the crater-scaling relationships quantitatively. The DEM simulations avoid limited low-gravity time, test conditions, vibration-caused noisy data in drop towers and parabolic flights, as well as stochasticities due to granular beds in labs, while allowing to perform *simulated experiments* in virtually any small-body environment. As each particle's state is recorded during simulations, collected data can be post-processed to compute not only crater size but also ejection properties during the process. This would then yield a complete test of the relationships under given conditions and allow filling the gap in the literature.

The DEM code employed in the study is called parallelized kd-tree gravity code (pkdgrav in short), a state-of-the-art parallelized granular mechanics simulator. pkdgrav treats particle–particle collisions through a soft-sphere discrete element method (SSDEM) (Schwartz et al., 2012). Through SSDEM implementation, pkdgrav handles multi-contact and frictional forces using dissipative and frictional parameters that allow mimicking the behavior of angular and rough particles. Originally developed for large-scale planetary formation studies, the capabilities of the code are now extended to simple geometric shapes and their interaction with the granular surface (Ballouz, 2017). The code has been tested extensively and calibrated for a variety of materials to represent granular behavior realistically throughout different studies (Michel et al., 2011; Richardson et al., 2012; Yu et al., 2014).

As noted, pkdgrav models an interaction between particles with a set of contact parameters. The SSDEM implementation of pkdgrav requires a spring coefficient that is determined primarily by the expected velocities of grains in motion (Schwartz et al., 2012). This is not apriori known, except for the case of free-fall, hence it was set to be impact velocity. Additionally, the user is required to provide normal and tangential coefficients of restitution (ϵ_n, ϵ_t, respectively), as well as coefficients of Coulomb, rolling and twisting frictions (μ_s, μ_r and μ_t, respectively). Instead of arbitrarily appointing these numbers, this study makes use of previously-calibrated values. pkdgrav was previously tested in impact experiments with glass-beads material (Richardson et al., 2012), as well as in simple avalanche experiments with similar-sized gravel materials (Yu et al., 2014), and subsequent simulations were performed to reproduce the apparent behavior. The values are reported in Yu et al. (2014) and Ballouz et al. (2015) and also summarized in Table 3.

At the study that those parameter values were reported (Ballouz et al., 2015), the twisting friction functionality in pkdgrav had little influence on particle–particle interaction, hence it is set to 0 (i.e. no twisting) and therefore not reported here in Table 3. In this study, the simulations were performed with the glass bead parameters. It was previously reported by Housen and Holsapple (2011) that low friction between glass bead particles results in amplified behavior, especially in ejection velocities (Housen and Holsapple, 2011). This will be discussed further in the paper.
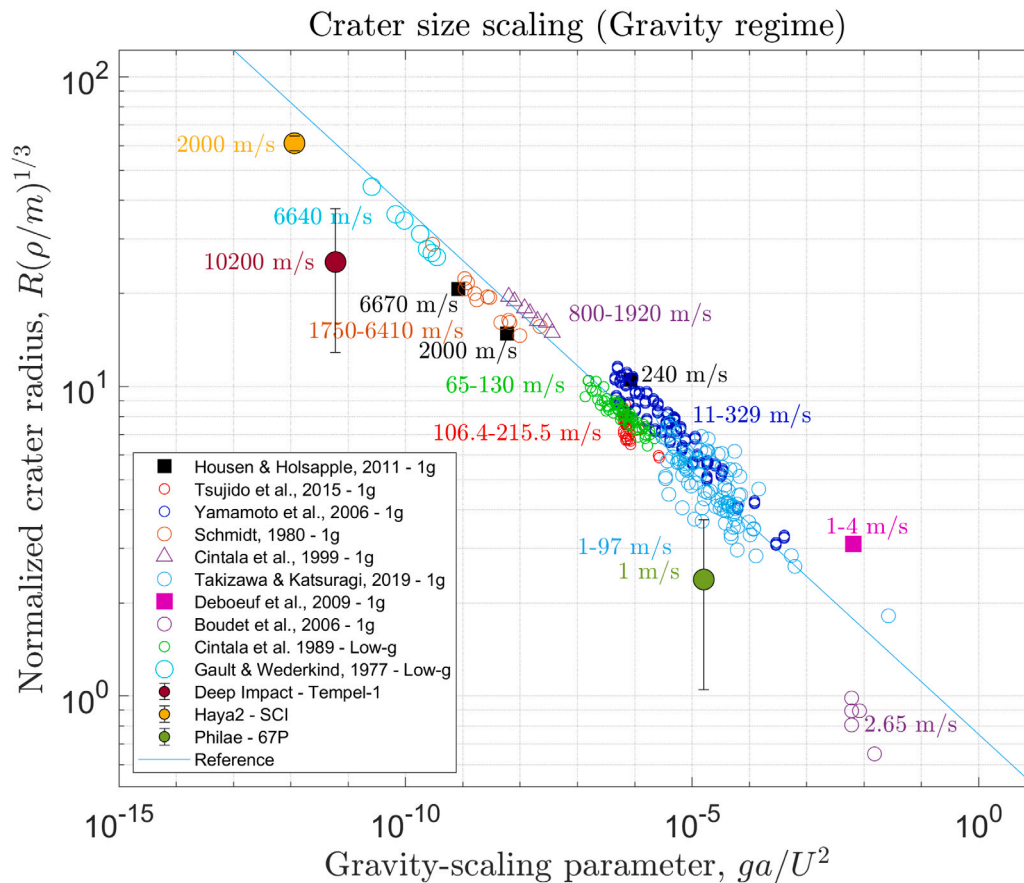
Fig. 3. Normalized gravity-regime crater sizes from different experiments.

Table 3
Summary of SSDEM material parameters (Ballouz et al., 2015). k_n value is calculated from Schwartz et al. (2012).

Parameters	Glass beads (GB)
ϵ_n	0.95
ϵ_t	1.0
μ_s	0.43
μ_r	0.1
k_n	75.25 kg/s^2

An illustration of the initial simulation set-up is presented in Fig. 4. A left-handed reference frame is used in the simulations, where positive z direction is opposite to the gravity vector, the y direction points in the out-of-paper (or *viewer*) direction, and x completes the triad. The DEM simulations were initiated with 38723 1-cm radius particles with a density of 1600 kg/m^3. While this particle is relatively large compared to millimeter-sized particle granular beds typically used in experimental studies, it is certainly within the range of sizes observed from the SCI crater during the Hayabusa2 mission (Wada et al., 2021), in the sampling site and among the ejected particles of Bennu during the OSIRIS-REx mission (Burke et al., 2021; Chesley et al., 2020). Even though it is a common practice to provide a slight variation in particle sizes to avoid ordered-packing, the particle size was kept the same throughout simulations to avoid the particle size effects in the impact outcome. A scaling relationship for particles is presented in Ballouz et al. (2021). The particle density is selected arbitrarily without targeting a specific material, but the selected value is an estimated value for porous carbonaceous material (Kuzmin et al., 2003). The particles were initially set for free-fall motion above a cylindrical container of 0.55 m in radius and 0.35 m in depth with the selected porosity of 35%. Simulated free-fall motion at $10^{-5}g$ (where g denotes the gravitational

acceleration on the surface of the Earth, i.e., $g = 9.81$ m/s^2) fills a 0.55 m radius cylindrical container up to 0.28 m, resulting in a final porosity of 39.04%. The bulk density of the final granular assembly then becomes 975.36 kg/m^3.

For a majority of the simulations, a single-sized, 5-cm radius spherical impactor was used. For the selected particle radius of 1 cm, this is roughly the minimum impactor radius to minimize the coupling effects in momentum and energy exchange, as suggested by Housen and Holsapple (2011). This argument will be tested later in this study with impactors of 1-cm (*i.e.*, equal to particle size) and 3-cm impactor. The container-to-impactor size ratio is 11, therefore suitable to eliminate the container-size effects (Seguin et al., 2008). Throughout the simulations, the density of the impactor is varied to observe the outcome of the impacts, especially to detect bouncing/submerging motion. Specifically, the impactor density, δ, was varied from one-tenth to about twice the bulk density of the impacted material, ρ.

Impact simulations are performed under $10^{-5}g$ created in the simulation environment by vertical impacts at speeds between 5 cm/s and 50 cm/s in the simulated regolith bed. It is worth noting that granular material subjected to low gravity levels and high shear rates can transition to a collision-dominated gas-like behavior, as reported in experimental studies and observational findings (Daniels, 2013). For the gravity levels and shear rates in our simulations, the target material appears to have a fluid-like response that is well described by crater scaling laws (see Section 5). However, it should be noted that at lower gravity levels and/or higher impact speeds, which were not explored here, the materials may behave more gas-like and it is unknown whether crater-scaling laws are still applicable.

The selected velocity range covers frequently-encountered impact velocities on small-body surfaces, and about the escape speed of Bennu, as well as OSIRIS-REx touchdown speed (Scheeres et al., 2019; Lauretta
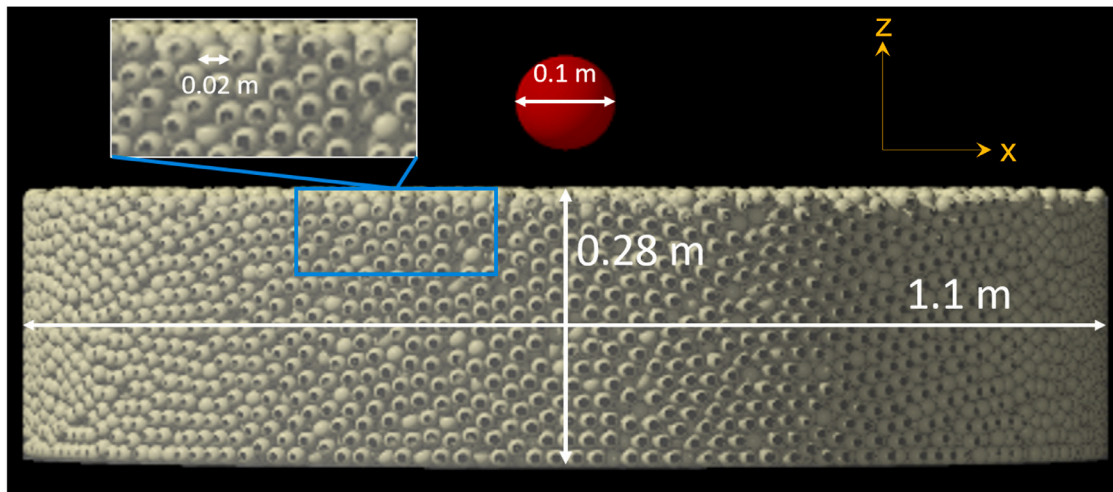
Fig. 4. Initial simulation setup.

et al., 2019; Lauretta and OSIRIS-REx TAG Team, 2021). Recall also that the cover of MINERVA-II landers impacted on Ryugu's surface at ~28 cm/s (Van wal et al., 2019), whereas the Philae lander impacted on 67P's surface at 1 m/s (Biele et al., 2015). MASCOT landing on Ryugu is estimated to occur at ~17 cm/s from spacecraft images (Scholten et al., 2019). The selected level of gravity is also approximately in the same level as the currently-visited asteroids Ryugu and Bennu, as well as previously-visited comets 67P and Tempel-1 and asteroid Itokawa. Note that the simulations result will not be presented for the cases U = 50 cm/s - δ = 1040 kg/m^3 and U = 50 cm/s - δ = 1910 kg/m^3 as the crater sizes are observed to overflow the container dimensions. The covered parameter space is summarized in Table 4.

Table 4
Covered parameter space during simulations.

Parameter	Value
a [m]	0.05
δ [kg/m^3]	100, 260, 347, 520, 1040, 1910
U [m/s]	0.05, 0.1, 0.25, 0.5
ρ [kg/m^3]	975.36
ρ_p [kg/m^3]	1600
r_p [m]	0.01
ϕ [%]	39.04
g [m/s^2]	9.81 · 10^{-5}

Among the previously-undefined parameters in Table 4, r_p and ρ_p are particle radius and density of the granular system, respectively. ϕ denotes porosity and g denotes gravity acceleration.

With the parameters presented in Table 4, a total of 22 simulations were performed. Two additional simulations were performed to test the effect of impactor-to-particle size ratio. The simulations were stopped at 350 s (or approximately after 6 min) for the impact speeds 0.05 and 0.1 m/s and 525 s (or approximately after 9 min) for 0.25 m/s and 0.5 m/s cases. It was found that particle speeds within the granular bed is less 1 mm/s within this time. The data collected at the end of a simulation is post-processed to extract the information related to cratering. At this stage, it is necessary to develop computational techniques to post-process the obtained data. Before presenting the results of the impact simulations, those computational procedures will first be outlined in the next section.

4.1. A procedure to detect crater size

In a laboratory setting, the size of a crater is often the easiest property of it to be measured. In general, because of small grain sizes, final crater figures appear like plastically-deformed solid materials. The same would appear in DEM simulations, too, provided that the impactor-to-particle size ratio is high, likely to be on the order of

hundreds or more. The impactor-to-particle size ratio is a rather small value of 5 for all of the simulations. Therefore, the final crater shape is discontinuous. The particle ejection is not radially-uniform due to the initial random packing which results in a circular-like discontinuous cavities on the surface. It is needed to scan the cavity radially in the x–y plane from the impact point, until the nearest particles are found at some radial distance, i.e., defined as crater radius. This poses a computational challenge to be addressed. A computational procedure outlined in Alg. 1 is therefore developed to determine crater radius and later its depth.

Algorithm 1 Crater radius detection algorithm

1: **procedure** CRATER RADIUS AND DEPTH(Initial state, Final state)
2:     Select grains within container dimensions and selected height
3:     Calculate radial, angular positions of particles, R_p, θ ▷ First, find crater radius
4:     Find highest particle's height, h_{max}
5:     **if** $h_{max} > 0$ **then**
6:         Select all particles from 1 cm below the initial height, h_0, to h_{max}
7:         Divide circular region of cylinder radius to 3, 6, 9 sections, n_r
8:         **for** n_r = 3, 6, 9 **do**
9:             **for** j = 1:n_r **do**
10:                 Find total number of particles in each region, n_p
11:                 **if** $n_p \geq 5$ **then**
12:                     Sort particles in ascending order of R_p
13:                     Select first five particles
14:                 **else if** $n_p < 5$ **then**
15:                     Select all found particles
16:                 **end if**
17:                 Apply a least squares to find crater radius $R_{cr}^{n_r}$
18:             **end for**
19:         **end for**
20:         R_{cr} = mean($R_{cr}^{n_r}$)
21:     **else**
22:         Warning: "Crater is either larger than the container dimensions or not formed at all. Check output"
23:     **end if**   ▷ Second, find crater depth
24:     Find particles with $R_p \leq 2r_p$ & $h_p < 0$
25:     Sort selected particles in descending h_p order
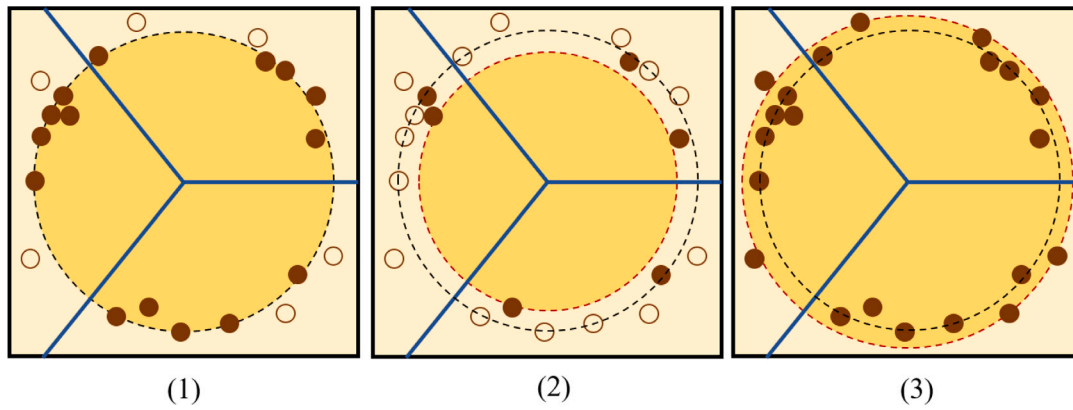26:   Select max(h_p) as crater depth d_{cr}
27: **end procedure**

Fig. 5. Overview of crater radius detection. In this case, the virtual container space is divided into three sections. Number of particles to be selected in each section affects the final crater size. (1) shows a final estimated crater with optimum number of particles found empirically during the study. (2) and (3) show under- and overestimated crater radii respectively.

In short, Alg. 1 selects displaced particles on the top few layers of the final crater and finds a circle that fits the best to closest particles to impact point. In this study, the first two layers with respect to the original unimpacted surface and particles in these layers are used to find crater radius. The circular region defined by the container radius is divided into a number of portions and the closest N number of particles are selected in each portion such that a proportionate particle selection can be ensured. A least-square method is then applied to find the best-fitting circle. This means that crater radius (or diameter) is defined on the original unimpacted surface as the apparent radius, not rim to rim, with final crater. The circular region is divided into at least three different numbers of section, *i.e.* three different circles are fit, and their mean is calculated as an additional layer of estimation. On the other hand, for example, the crater depth is computed rather straightforwardly: The particles whose positions are below the original granular layer and within $2r_p$ from the impact point are determined, sorted in descending height order, from which the maximum particle height is determined to the crater depth. Note that the formed craters are assumed circular paraboloid in shape following the simple crater definition of Melosh (1989), and the shape can be described with the following elliptical paraboloid equation (opening upwards):

$$z = \frac{x^2}{c_1^2} + \frac{y^2}{c_2^2} \qquad (13)$$

where c_1, c_2 are semi-major and semi-minor axis lengths of top elliptical surface of the paraboloid. For circular paraboloid, c_1 and c_2 are equal to R.

One of the main challenges with the presented approach is that, due to the inherent nature of the least-squares method, the best-fitting circle shifts towards regions where more particles are found. Therefore, selecting appropriate number of sections and particles in each section is imperative. If more particles are selected, then crater size will naturally be overestimated and if, on the other hand, too few particles are selected, then the crater radius will be underestimated. Moreover, a blind selection of closest N particles would not work either, because it would only result in a shifted circles towards particles in most densely-populated part of the final crater, as a crater is often not perfectly symmetrical. Both number of sections and number of particles in each portion are found empirically. The procedure is illustrated in Fig. 5.

In the analysis of generated data, three different numbers of sections, 3, 6, and 9 (scanning 120°, 60° and 45°) are selected to mitigate over- or underestimation. $N = 5$ particles are selected at each portion in order to maximize the fidelity in the least-square results. If, for a given section, at least 5 particles are not available, then the maximum number particles from that section is selected. As stated earlier, one

crater radius is fitted in each step. For example, when a crater is separated into three sections (i.e., each scanning 120°), 5 particles closest to the impact point are selected, and a circle is fitted with the total of 15 particles. This procedure is repeated for 6 and 9 sections with a total of 30 and 45 (or the maximum number of available) particles to fit a circular crater radius. An example crater radius result from this algorithm for the impact case with $U = 0.1$ m/s and $\delta = 1910$ kg/m^3 can be seen in Fig. 6.

As one can see in Fig. 6, finally-detected crater represents the observed crater well (left figures), and the selected particles (red dots in top-right figure) are evenly distributed to represent the crater radius. Recall that crater radius is defined on the original, unimpacted surface. The heights of the selected particles are also close to 0 (bottom-right), and calculated from this point, therefore appropriate for comparison to experimental data. Final crater radius is 0.33 m and final crater depth is 0.10 m in the case presented in Fig. 6. The residual sum of squares (RSS) value is 0.00055 m, or 0.16% of the crater radius. During crater size estimations, the RSS values are generally found to be less than 10%, except a single case, where the RSS was found approximately 12%, in which the impactor moves both vertically and laterally, and the final crater shows a pronounced ellipticity. All in all, the applied algorithm appears to be robust while simple and versatile enough to modify when necessary, *e.g.* when there are emptier regions or the shape is more elliptical.

4.2. Ejecta properties

Ejecta properties includes ejection speed and ejected mass. *Ejection* is defined as a particle's departure from the initially-defined top level of the container, *i.e.*, positive out-of-plane motion from the plane defined by the x and y axes, in the container reference frame, as presented in Fig. 4. The process of determining ejecta velocity and mass rather more straightforward compared to crater sizes, but the subtleties of the data collection will be explained.

4.2.1. Ejection velocity

pkdgrav outputs position, velocity, rotation and attitude information of particles after an user-inputted number of steps to avoid high data-load otherwise. In this study, the integration time step is ~0.7 ms, and the output time step is selected to be 2500 steps which means that a particle step file was generated approximately at every ~1.8 s of the motion. Because of the discrete data collection, it is possible that, between two consecutive outputs, particles that are initially buried in the granular bed may be ejected already in the next data output. This practically occurs for all ejected particles as it is not feasible to control the precise ejection time for each particle. Therefore, first, the discrete data files are scanned and ejected particles are tracked

a = 0.05 m, U = -0.10 m/s

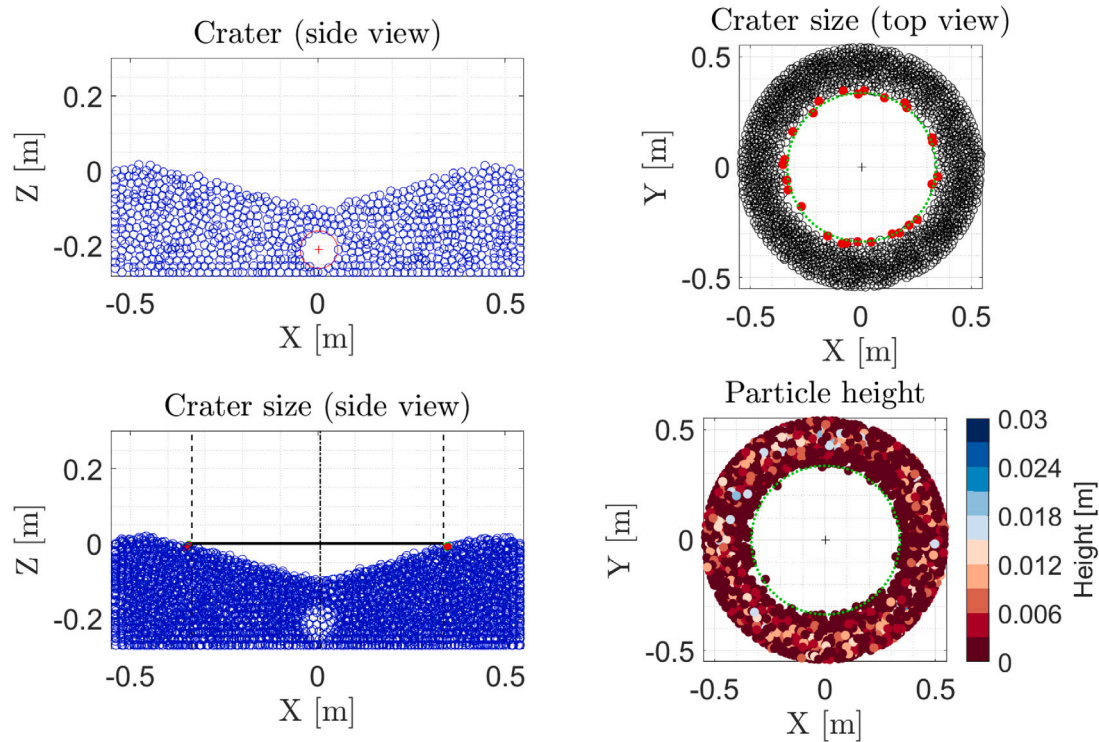**Fig. 6.** An example result from crater-size detection algorithm for the example impact case: $U = 10$ cm/s, $\delta = 1910$ kg/m³. Upper left: Side view of the crater. Upper right: Top view of the first 2 cm of the post-impact granular bed, with the selected particles in red and fitted circle for crater in green. Lower left: Side view of the fitted crater with crater boundaries (dashed lines), the center (dashed dotted line), crater top (black line), and the selected particles for the crater size (red). Lower right: Particle height after crater formation with respect to the pre-impact granular bed. The color bar shows height from 0 to 3 cm in red to blue. (For interpretation of the references to color in this figure legend, the reader is referred to the web version of this article.)

throughout all data outputs. This procedure is significantly simplified with the pkdgrav capability of assigning each particle an ID number based on their order of generation when they are first initiated above the virtual container. Then, the motion of the mid-flight particles are integrated backwards in time analytically until the surface, in order to find the precise ejection time and state. Particles are assumed to follow a ballistic trajectory without interacting with each other once they are ejected (see Fig. 7).

In order to compare the processed data with the crater-scaling relationships, a mean velocity profile is generated as a function of distance. This was done by dividing the maximum ejection distance with a number of concentric circles centered at the impact point, and calculating the mean of velocities observed within the circular section between two circles. 15 circular portions are found empirically to be the best representing velocity profiles obtained. The ejection velocity of the example impact in Fig. 6 is provided in Fig. 8.

According to Fig. 8, vast majority of particles have ejection speeds less than 2 cm/s. The highest speed particles are close to the impact point, as expected from these kinds of impacts. Surrounding the impact point, the particles mostly have ejection speeds 4 cm/s or below. The two highest speed particles have ejection speeds higher than 8 cm/s is also right next to the impactor. Ejection distance of particles, their ejection angles and approximate ejection time after the impact are presented in Fig. 9.

According to Fig. 9, material ejection can be observed nearly up to a minutes after the impact, albeit with below-cm/s level velocities. The ejection velocity is decreasing with the distance from impact point as expected. The immediate surrounding of the impact point is where the highest speed particles are located. The highest ejecta velocity is about 9 cm/s or 90% of the impact speed. A few cases with 3–5 cm/s can also be seen. In this specific case, the ejection velocity decreases

below centimeter-per-second level within 10 cm from the impact point or approximately 5 cm from the impactor edge. The lowest velocity ejecta that leave the surface in the outermost regions are not launched in the same way with those closest to the impact point, but rather pushed up above the initial granular layer without any ballistic flight. This is observed during the simulations and can also be inferred from their below cm/s speed, shown in the velocity profile as a function of distance in Fig. 9.

The ejection process largely ends approximately when the crater radius is reached; however, some grains are observed to move above the initial defined container level, through the end of the cratering process with very low speeds, shown in Fig. 9a. Given that those particle speeds are on the order of mm/s, it can be inferred that they are likely pushed through some sort of chain of impacts between particles, either within the granular bed, or through the particles that fall back after ejection. Because of this, the ejection angle, measured from local horizontal, of the particles with very low ejection speeds are rather randomized, *i.e.*, both very shallow and steep angles are observed throughout the ejection profile, as shown in Fig. 10b. On the other hand, within the initial crater radius, ejection angle becomes shallower with the increasing radial distance from the impact point. A similar trend is also observed in high-speed cratering (Cintala et al., 1999).

The mean ejection velocity profile is shown in Fig. 10. A decrease in mean velocity can be found in Fig. 10a with the distance from the impact point. Note that even though the highest speed in this specific case is ~9 cm/s, the average is approximately 2.25 cm/s within the annular ring that this particle is in. Then, the decrease continues until slightly below 5 mm/s at the crater radius and down to 1 mm/s or lower as the radial distance approaches to the maximum ejection distance found, which is approximately the container radius in this case. The ejection angles, presented in the histogram in Fig. 10b, show that most
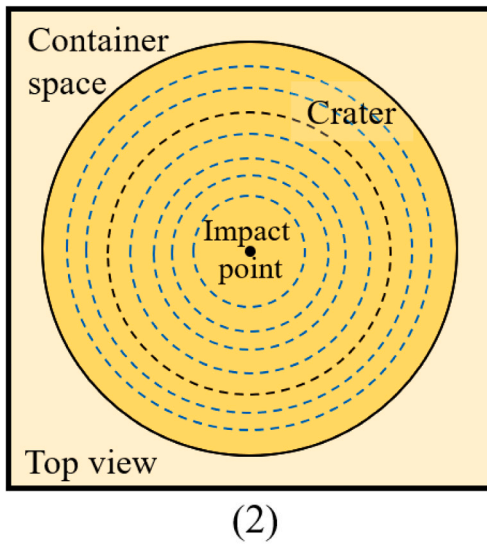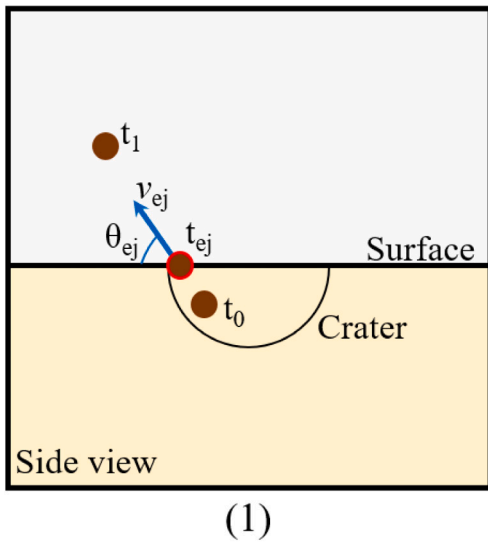
Fig. 7. Extraction of ejection speed and angle. (1) Between two `pkdgrav` outputs (at t_0 and t_1), its ejection state may not be determined, therefore it is propagated backwards analytically to surface level. Ejection angle is calculated from local horizontal. (2) After all ejection states are determined, the container space is divided into annular rings by concentric circles, within which mean ejection speed is determined.

Fig. 8. Top view of ejected particles with their ejection position and velocity, for case with U: 10 cm/s, δ: 1910 kg/m^3. Each point represents an ejected particle. Color denotes ejection speed ranging from 0 cm/s (blue) to 9 cm/s (orange). (For interpretation of the references to color in this figure legend, the reader is referred to the web version of this article.)

particles depart surface with angles between 40° and 60° with average around 50°. However, a considerable amount of ejecta have angles greater than 60°. Those high-angle ejecta are primarily the higher speed particles immediately next to the impact point in the beginning of cratering or very low-speed particles, pushed up afar from the impact point at later stages of cratering, from the interpretation of Fig. 9b.

Detailed ejection velocity information can be obtained through the computational post-processing procedures developed for the dedicated DEM simulations. Similar to the above results, the procedure is applied to all impact cases to investigate their ejection velocity profile. Before presenting those results, the procedures specific to ejected mass will be outlined in the next section.

4.2.2. Mobilized mass

The computational procedure to extract the ejected mass is also relatively straightforward. Each ejected particle can be registered with the procedure outlined in the previous subsection. Additionally, in this
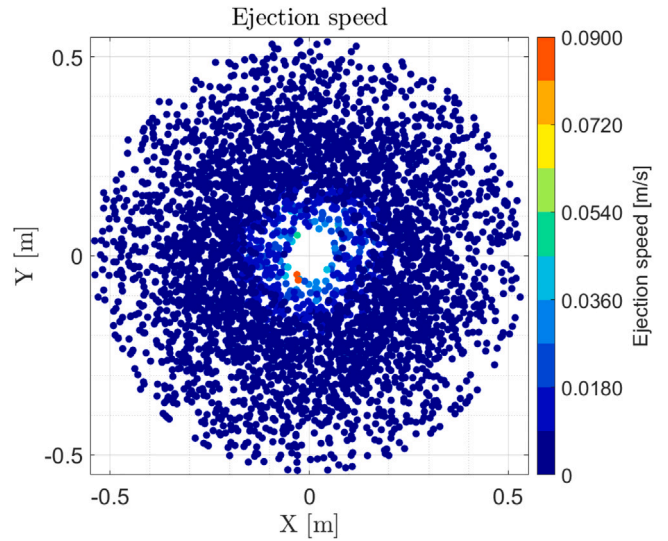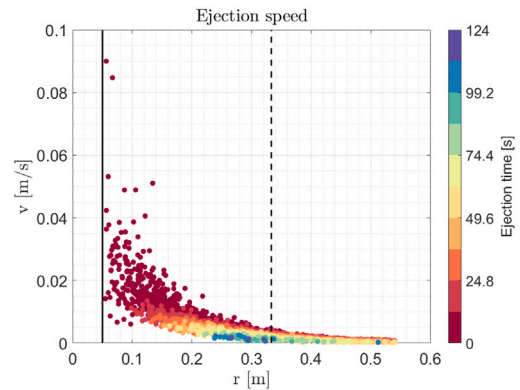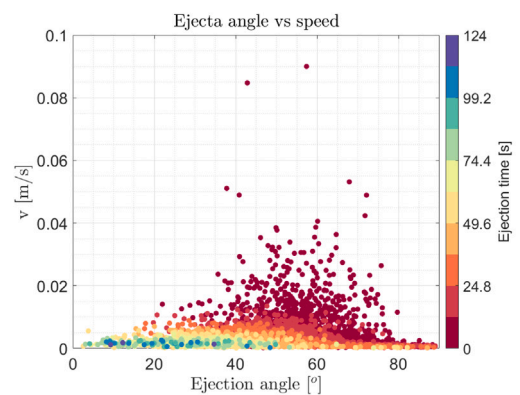

(a) Speed vs Distance

(b) Angle vs Speed

Fig. 9. Velocity of ejected particles compared to distance from impact point, for case with U: 10 cm/s, δ: 1910 kg/m^3. Each point represents a simulated particle. Color denotes ejection time ranging from t = 0 s (red) to t = 124 s (purple). Black line denotes impactor radius, black dashed line denotes the fitted crater radius. (For interpretation of the references to color in this figure legend, the reader is referred to the web version of this article.)
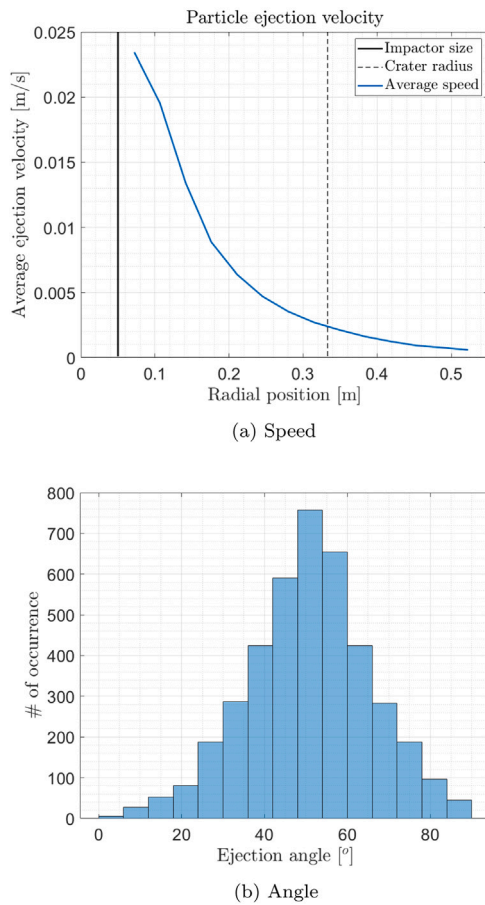
(a) Speed

(b) Angle

Fig. 10. Ejection dynamics for the case U: 10 cm/s, δ: 1910 kg/m^3. Left panel: Average ejection speed as a function of radial position from the impact point. The blue curve denotes the average speed. The vertical solid and dashed lines represent the impactor size and the crater radius, respectively. Right panel: A histogram of the ejection angle of particles. (For interpretation of the references to color in this figure legend, the reader is referred to the web version of this article.)

study, the ID numbers of particles that are initially within the circular paraboloid crater boundaries, defined by Eq. (13), but not ejected, were also registered in order to analyze the relative mass of *ejected* and *pushed-down* material within the impact generated crater. Hence, instead of ejected mass, the term *mobilized mass* is adopted. An example of this analysis can be seen in Fig. 11.

In Fig. 11, the polyhedral shape of the final crater is generated with MATLAB's `alphaShape` function, which uses a set of input points to create a two- or three-dimensional shapes (Edelsbrunner and Mücke, 1994; Ballouz et al., 2019). The detection of a particle's position inside or outside of the crater bowl is also made with the functionality of the same MATLAB function. According to the figure, initial few layers of particles underneath the impactor are ejected, only then particles are pushed further down. In this specific case, majority of the materials that are initially in the crater bowl are ejected.

Thanks to the quantitative framework provided by the DEM simulations, each mobilized particle can be tracked. In order to make a comparative study with the existing cratering experiments in high and low speeds, the data analysis needs to be made for ejected particles only. Specifically, the cumulative mass of ejected material with velocity greater than some given velocity v is computed. Fig. 12 shows the ejected mass in the example impact case with $U = 10$ cm/s, $\delta = 1910$ kg/m^3.

As seen in Fig. 12, total ejected mass is about 15 kg. The mass value decreases as the ejection speed increases, in agreement with the

ejection speed results, in which the highest speed ejecta is restricted to the immediate surrounding of the impact point, hence in smaller amounts. The smallest amount of mass is less than 1 kg occurs for the ejection speeds at the highest average speed ejecta, i.e., 2.25 cm/s.

To sum up, in this section, DEM simulations and the computational procedures used in this study are outlined. A single impact case is used as an example to demonstrate a variety of quantitative analyses that were performed. In the following section, those analyses will be presented for a whole set of impact low-speed impact simulations performed.

5. Results

The complete set of results for all simulations are tabulated in Table A.6. As noted earlier, impactor density δ and impact speed U are systematically varied during the simulation while keeping the other parameters fixed. First, the simulation outcomes of those will be discussed as presented in Fig. 13.

Two distinctive behaviors, which are called bounce and submerge here, are observed during the study that are primarily separated based on the impactor density. The former, bounce, is defined as the motion in +z direction (*i.e.*, away from the granular bed), as defined in Fig. 4, after a contact without significant penetration. The latter, submerge, is the more typically observed in cratering of the two, and defined as full or partial penetration (*i.e.*, motion in −z direction) that halts the motion of the impactor in the simulated granular bed.

Regardless of the impact speed considered, the impactor bounced off the surface at low density values. As it will be investigated later, those cases also result in impact craters, but generally smaller in size. Similar bouncing behavior is observed in the experimental data presented in Colwell (2003) and Brisset et al. (2018) with spherical impactors, and in the simulation data presented in Zacny et al. (2018) for a cylindrical impactor mimicking a spacecraft sampler horn. The latter work also attempted an analytical explanation for the behavior (Zacny et al., 2018). In the simulations here, the impactor density values that result in bounce is 100, 260, 347 kg/m^3, which means $\rho/\delta >$ 3. The impactor submerges for $\rho/\delta < 3$. It can then be stated that the bounce/submerge transition occurs at approximately $\rho/\delta \approx 3$. It is likely that this ratio needs further confirmation from experiments and simulations with different material properties and impactor density values. When $\rho/\delta < 3$, typical submerge behavior is observed with the impactor penetrating the simulated granular bed, penetration depth scaling with impactor density. However, it is worth noting that, because of the container depth of the simulated granular bed, penetration depth may be limited at the impacts with higher density impactors for $\rho/\delta <$ 3. Finally, even though two distinct behaviors are observed, the submerge behavior near the transition density resembles floating, moving not only vertically but also laterally on the surface during cratering and stay only partially buried in the end. This is also considered as submerge for the quantitative analysis. It is also worth noting that δ/ρ is not only parameter that drives the bouncing behavior, and it was shown that higher density impactors can also ricochet off the surface if their impact angles are below (or above, depending on the direction from which the impact angle is measured) some threshold value (Maurel et al., 2018; Thuillet et al., 2018; Çelik et al., 2019).

In the next subsections, the results for all impacts, irrespective of their qualitative outcome, will be discussed from the crater scaling relationships perspective and in comparison with the previous experimental literature.

5.1. Crater size

The crater sizes are calculated from the simulation data with the post-processing approach outlined in Section 4.1. However, before attempting to calculate the scaling relationship, it is also of interest whether separation between the data points are due to variation in
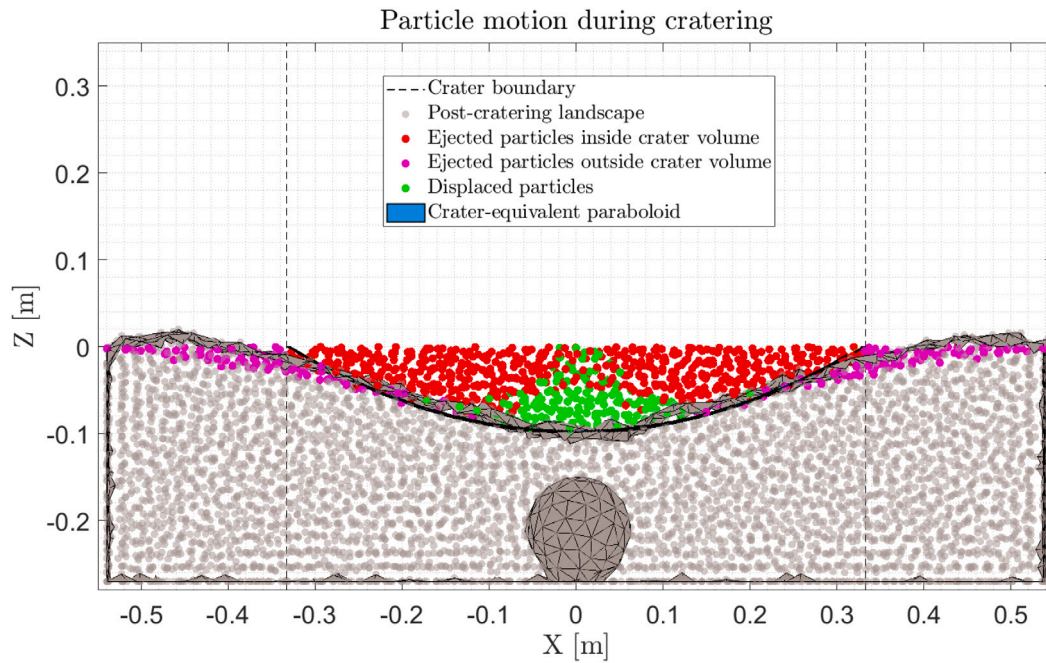
Fig. 11. Cratering landscape for the impact case: U: 10 cm/s, δ: 1910 kg/m³. Dashed line marks the crater size as found by the algorithm outlined in Section 4.1. Light brown color shows the particle positions and the post-impact shape of the crater. Red and magenta colored particles are ejected particles from inside and outside of the final crater bowl, respectively, and shown in their pre-impact positions. Green particles are displaced towards the granular bed, again shown in their pre-impact position. Blue surface is the crater-equivalent paraboloid, appearing as parabola in 2D. (For interpretation of the references to color in this figure legend, the reader is referred to the web version of this article.)
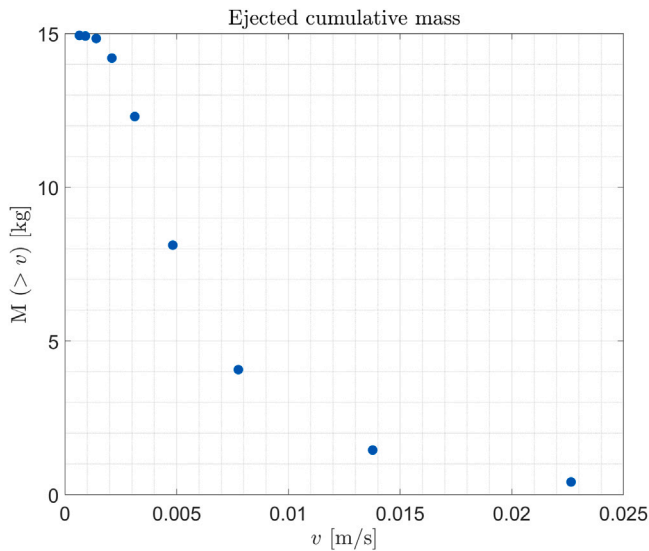

Fig. 12. Cumulative ejected mass with velocity greater than v for the impact case: U = 10 cm/s, δ = 1910 kg/m³.
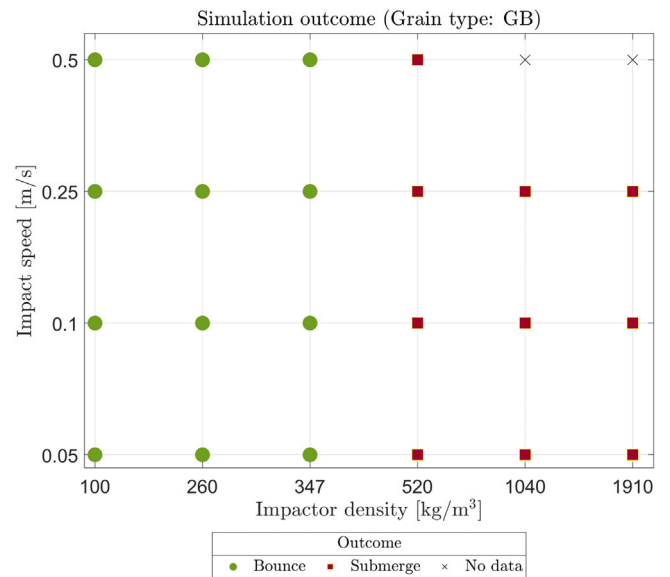

Fig. 13. Qualitative outcomes in the DEM simulations outlined in Section 4. Green circles show cases where impactor rebounded, whereas red squares show impactors that submerged in the granular bed at the end of each simulation. Gray crosses show where currently there is no simulation data.

impactor density. Previously (Housen and Holsapple, 2011) have noted the variation in ejecta velocity with varying impactor density in a limited set of experiments, but also stated the need for additional experiments (Housen and Holsapple, 2011). Thus far, only Tsujido et al. (2015) performed a dedicated experimental study on impactor density variation in impact cratering (at $U \sim 200$ m/s) (Tsujido et al., 2015), in which the authors noted a weak dependency of crater sizes to density variation. Therefore, before calculating the empirical relationship, the impactor-density dependency will be investigated in the $\pi_4 - \pi_R$ space

with the set of crater sizes for the available velocity and impactor density values, as presented in Fig. 14.

Fig. 14 shows dimensional crater radius R and $\pi_R = R(\frac{\rho}{m})^{1/3}$ as a function of $\pi_4 = \rho/\delta$. It is shown that, for a given impact speed, craters are larger for denser impactors, except two outlier cases at 25 cm/s and 50 cm/s. However, when the π_R value is considered, it is observed that it has a slight variation but is roughly constant except at the extreme values of density, as well as a single case at 50 cm/s. While the results
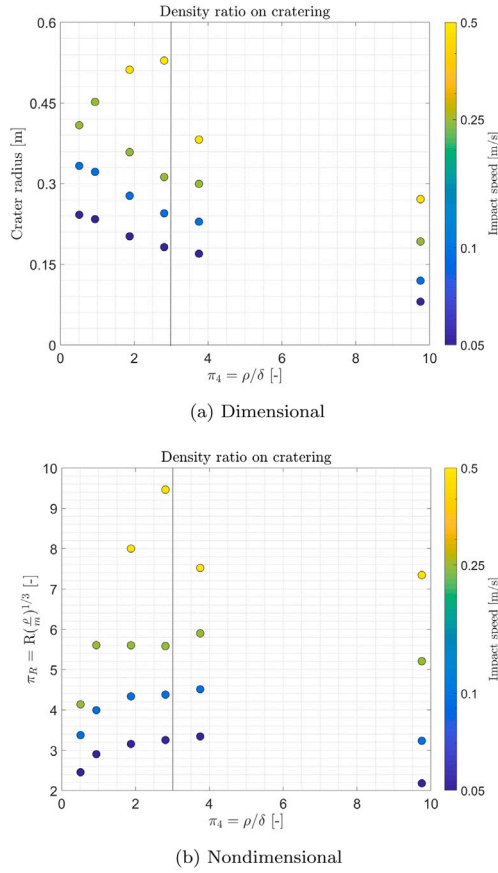
Fig. 14. Effect of target-to-impactor density ratio (π_4) in crater sizes (left panel) and π_R (right panel). Purple, blue, green and yellow colors denote 5, 10, 25, 50 cm/s impact speeds. Black vertical line denotes bounce/submerge transition density $\rho/\delta \approx 3$ found in this study. (For interpretation of the references to color in this figure legend, the reader is referred to the web version of this article.)

in Fig. 14 are admittedly not enough to completely rule out the effect of impactor density, the dependency appears to be weak at least for the impacts simulated here. The power law expression is $\pi_R = 4.48\pi_4^{0.07}$, suggesting a weak relationship between π_R and π_4. Further dedicated experimental and simulation work appear to be necessary to assess the effect of impactor density on cratering. Therefore, for the rest of the paper, the effect of impactor density will be assumed negligible.

It is now possible to look into the cratering results nondimensional crater radius (π_R) as a function of gravity-scaling parameter, π_2, as shown in Fig. 15.

A distinctive feature is present in Fig. 15: The lower the π_2 values are (*i.e.*, higher impact speed) the larger the crater is for a given δ, here represented by impactor mass, m. Among different δ values, higher δ values result in larger craters. This is due to the larger penetration depth, which makes more materials to be mobilized from the crater cavity. Among higher impactor density values, there is a case at 25 cm/s where an outlier case occurs. A larger crater that can form at 25 cm/s may have been stopped by the container boundaries at the outlier case. On the other hand, there is in general a clustering among the crater sizes at the impactor densities that result in bouncing, except at 100 kg/m^3. At 100 kg/m^3, the craters are very small compared to those at higher δ, hence resulting smaller π_R values.

In order to calculate the crater-scaling relationships, first consider the following expression from π-scaling relations provided in Section 2, without the density-related π_4 term, as it is assumed negligible:

$$R\left(\frac{\rho}{m}\right)^{\frac{1}{3}} = K_R\left(\frac{ga}{U^2}\right)^{-\frac{\mu}{2+\mu}} \tag{14}$$

In π-scaling terms, the equation would take the following form:

$$\pi_R = K_R\pi_2^{-\alpha} \tag{15}$$

from Eq. (14), following equality can be found:

$$\alpha = \frac{\mu}{\mu+2} \Rightarrow \mu = \frac{2\alpha}{1-\alpha}$$

where μ is a material-dependent exponent (Housen et al., 1983). μ is also related to whether impactor momentum or impactor energy drive the crater radius (Housen et al., 1983). μ is usually found ~0.4 for dry sand in gravity-regime cratering and ~0.55 for impacts in water (Housen and Holsapple, 2011). In this study, the following relationship is computed with the best fit to all data presented in Fig. 15:

$$\pi_R = 0.69\pi_2^{-0.219} \tag{16}$$

In cratering experiments thus far, the procedure to find μ usually follows similar steps except specific aspects of the problem, *e.g.*, impactor density. This is because impact speeds are generally high, or the combinations of the involved parameters are such that experiments are similar with impactors fully submerging. Even bouncing results are limited to few recent studies, *e.g.* in Brisset et al. (2018), Takizawa and Katsuragi (2020), Wright et al. (2020) and Joeris et al. (2021). However, in the simulations here, cratering occurs with two distinct impactor behavior, as described in the previous subsection. Therefore, multiple μ values can be computed. In this study, the following relationship is obtained for the craters formed in the cases where the impactor rebounded:

$$\pi_R = 0.72\pi_2^{-0.222} \tag{17}$$

The values are tabulated in Table 5.

Table 5
μ values obtained from the simulated craters. R^2 denotes the goodness of fit.

#	K_R	μ	R^2	Remark
1	0.69	0.56	0.888	All data
2	0.72	0.57	0.896	Bouncing cases only

The use of all crater data available results in a μ value of 0.56 —- scaling exponent similar to water (Housen and Holsapple, 2011). The μ value is also similar for the cases the impact results in bounce. The μ value is between 1/3 and 2/3, such that it is consistent with the expectations from the crater scaling relationships (Housen and Holsapple, 2011), and close to impact energy scaling. The ν value, describing the impactor density relationship, is calculated 0.34 using Eq. (8) with $\pi_4^{0.07}$ presented earlier. The ν value is close to the typically considered value 0.4, indicating weak dependency to the impactor density. The μ value found here is higher than the generally-accepted ~0.4 for sand or cohesive soil (Holsapple and Housen, 2007). Previously Tsujido et al. (2015) found similar μ values (*i.e.*, ~0.57) from the impact experiments at relatively low speeds (~100–200 m/s) and varying δ between 1100 and 11 000 kg/m^3. The authors have not provided dedicated explanation for their higher μ values but speculated that the effects of relatively low speed and impactor density (Tsujido et al., 2015). Moreover, Cintala et al. (1989) found μ as 0.444 at relatively low-speed impacts (65–130 m/s) under reduced gravity (Cintala et al., 1989). On the other hand, it was stated in Housen and Holsapple (2011) that low friction between particles generally result in larger craters with increased ejecta velocities (Housen and Holsapple, 2011). In the same work, the authors provide the example of Yamamoto et al. (2006) work, in which $\mu = 0.45$ is found. This is indeed the case in the simulations in this paper, where DEM glass beads parameters exhibit the angle of repose angle of 20°, on the contrary to ~40° in gravel parameters (Yu et al., 2014). Combined with low gravity, low friction between granular particles may be the reason for higher μ values. In the DEM context, low energy dissipation due to the high coefficient of restitution value between particles may have resulted in larger craters. Previously, Wada et al. (2006) performed impact simulations
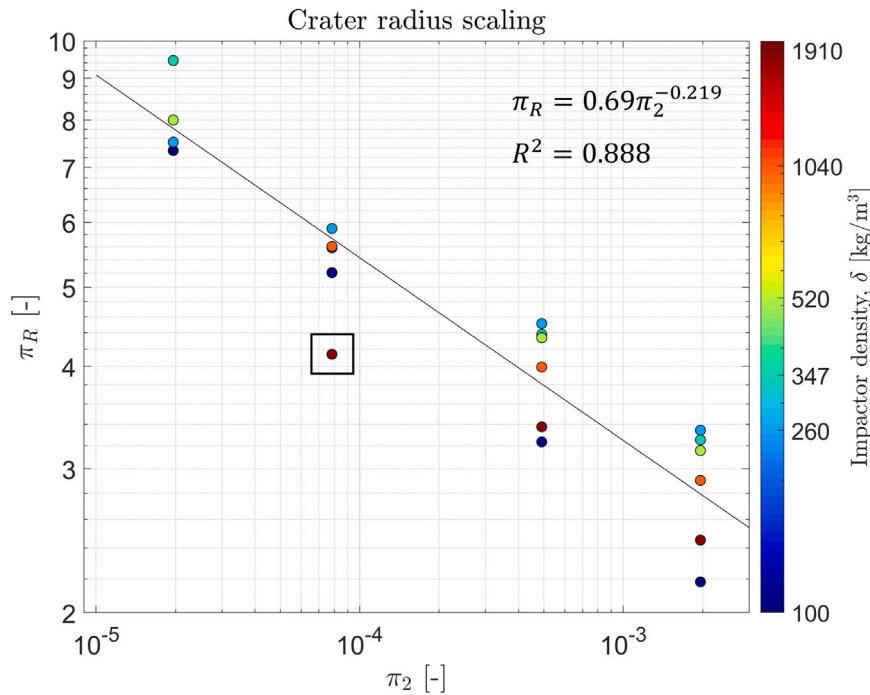
Fig. 15. Normalized crater radius ($\pi_R = R(\frac{\rho}{m})^{1/3}$) as a function of gravity-scaling parameter ($\pi_2 = \frac{ga}{U^2}$). Color denotes impactor density values $\delta = 100$ kg/m³ to $\delta = 1910$ kg/m³ from blue to red. The boxed result shows an outlier. The best fit to the data (black line) results in the empirical relation $\pi_R = 0.69\pi_2^{-0.219}$. (For interpretation of the references to color in this figure legend, the reader is referred to the web version of this article.)

at a few hundreds of m/s speed under Earth gravity and found similar results (i.e., $\mu \sim 0.4$) as dry sand. Wada et al. (2006) discussed that high coefficient of restitution and low coefficient of friction in the simulations result in larger craters. This is also the case here, where the coefficient of restitution and of friction values are 0.95 and 0.1, respectively. This result was also observed by Çelik (2020) in impact simulations with gravel-type parameters (i.e., $\epsilon_n = 0.55$) for under microgravity with impact speeds at 1–50 cm/s. It can then be expected that the higher energy dissipation would result in smaller craters, which would eventually drive μ to lower values. On asteroids, a coefficient of restitution value of 0.57 ± 0.01 is observed from the motion of one of the reimpacted particles on Bennu (Chesley et al., 2020), while Durda et al. (2012) inferred much lower values between 0.09–0.18 from their dynamical simulations of backtracking ejecta depositions from the craters of Eros' surface. Moreover, on the surface of Itokawa, Yano et al. (2005) reported a coefficient of restitution value of 0.85 from the touchdown of the Hayabusa spacecraft—a much higher value than that on Bennu and Eros. Van wal et al. (2019) also estimated the coefficient of restitution on Ryugu between 0.6 and 0.8 from the surface motion of one of the MINERVA-II rovers. It appears then that the uncertainty on the coefficient of restitution value on small-body surfaces is high, even within the same type of asteroids (Eros and Itokawa are both S-type asteroids). Then, the glass-beads parameters used in this study represent a rather more idealized case compared to the real small-body surfaces, which may be the reason for the results of this study. Finally, even though the container size is selected such that its effect is minimized, the container effect on crater formation may not be fully mitigated, especially at larger impact speeds where crater sizes are larger.

One can also investigate crater radius result from impact energy perspective, as shown in Fig. 16.

It appears that the crater radius is correlated with impact energy. If the relation is described as a power law, the crater size would scale with $1.014 \times E^{0.217}$, where E is impact energy. This result is very close to $\sim E^{0.226}$ found in De Vet and De Bruyn (2007), in which the authors performed impact experiments at 0.6–4.4 m/s under Earth gravity (De
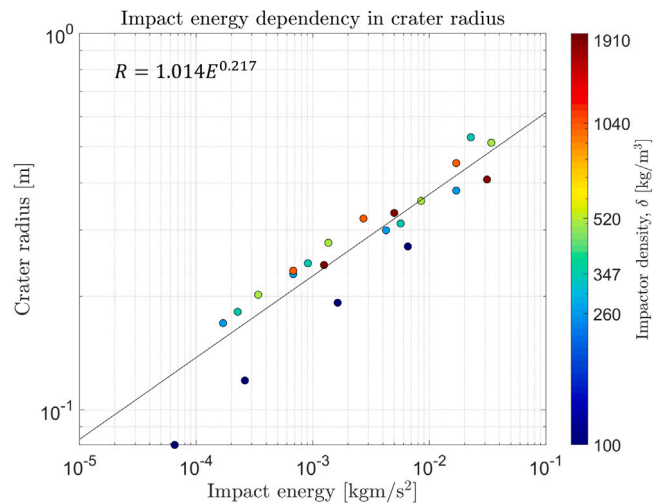

Fig. 16. Crater radius as a function of impact energy. Color denotes impactor density values $\delta = 100$ kg/m³ to $\delta = 1910$ kg/m³ from blue to red. The best fit to the data (black line) results in the empirical relation $R = 1.014E^{0.217}$, with the goodness of fit value (R^2, *not* the square of radius) of 0.884. (For interpretation of the references to color in this figure legend, the reader is referred to the web version of this article.)

Vet and De Bruyn, 2007). However, De Vet and De Bruyn (2007) have also included a particle-size dependent term for crater sizes (De Vet and De Bruyn, 2007). Moreover, a similar scaling exponent has also been calculated in low-speed impact experiments of Takizawa and Katsuragi (2020) and other works therein under Earth-gravity. From the reported literature in Table 2, the energy-scaling has also been investigated in Yamamoto et al. (2006) and Cintala et al. (1989) for relatively low-speed cratering experiments under Earth- and low-gravity, respectively and the scaling exponent of ~ 0.19 is recovered. Therefore, it can be stated that energy-scaling results also hold for low-speed impacts under low-gravity.
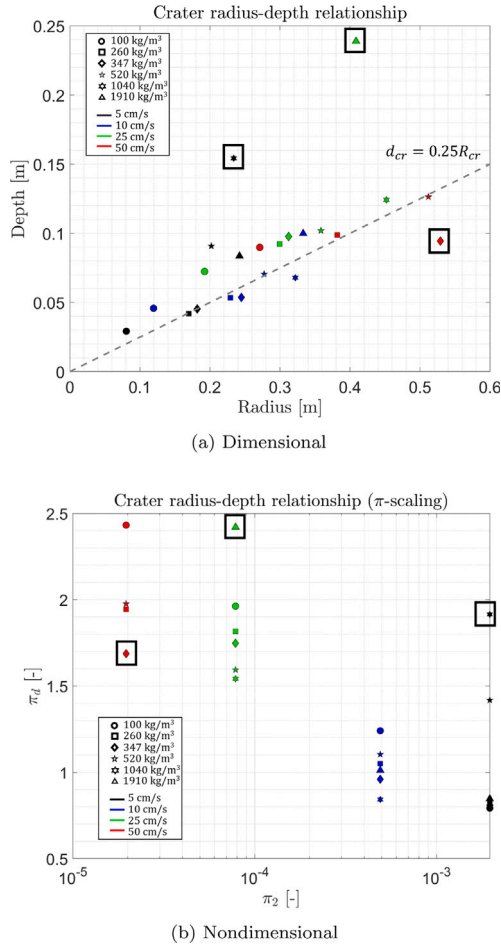
(a) Dimensional

(b) Nondimensional

Fig. 17. Crater radius-depth relation. Left figure shows dimensional crater radius against dimensional its depth. The gray line is drawn for $d_{cr} = 0.25 R_{cr}$. Right figure shows the same in $\pi_2 - \pi_d$ space. In both figures circle (100 kg/m³), square (260 kg/m³), diamond (347 kg/m³), five-pointed star (520 kg/m³), six-pointed star (1040 kg/m³) and triangle (1910 kg/m³) represent different density values. Black, blue, green and red colors represent the impact speeds 5, 10, 25 and 50 cm/s, respectively. Boxed results are outliers in both figures. (For interpretation of the references to color in this figure legend, the reader is referred to the web version of this article.)

Crater depth will be the next parameter to be investigated. This is done so in relation to crater radius and for both dimensional and nondimensional crater radius π_R. For the latter a nondimensional crater depth is defined as follows:

$$\pi_d = d_{cr}\left(\frac{\rho}{m}\right)^{\frac{1}{3}} \tag{18}$$

and the results of crater depth analysis are presented in Fig. 17.

The outlier data is boxed in Fig. 17. Recall that in this study, not only penetration, but also bouncing is observed. It is observed that in certain impact speed-impactor density combinations, the impactor did not fully penetrate the particle bed, but first partially penetrated then moved laterally in the bed at a depth, increasing the final crater size while decreasing the depth. This also resulted in erroneous detection of crater depth with the post-processing procedure outlined in previous section, hence the outlier data. The observation of this once again highlights the complexity of the cratering in this regime.

The rest of the data, on the other hand, presented a relatively orderly linear trend with d_{cr}/R_{cr} values varying around 0.25. Although the data appear to be scattered, one could also notice individual linear trends in each density values. Comparing with other works in the literature, Sugita et al. (2019) reported crater depth-to-radius ratios between 0.28 to 0.4 (Sugita et al., 2019), whereas Barnouin

et al. (2019) reported the same ratio as 0.32 for (Barnouin et al., 2019). In the experimental literature, Yamamoto et al. (2006) found d_{cr}/R_{cr} ~0.22–0.28 for impacts at 11–329 m/s impacts (Yamamoto et al., 2006). In a similar impact speed regime, Thuillet et al. (2020) reported depth values on the higher end of 0.6–0.65, but explained the result with incomplete cratering formation (Thuillet et al., 2020). On the other hand, Tsujido et al. (2015) reported d_{cr}/R_{cr} ~0.67–0.8 at ~200 m/s impacts. Tsujido et al. (2015) values are even higher than those achieved in astronomical impact craters, stated in Melosh (1989) as d_{cr}/R_{cr} ~0.5–0.67 (Melosh, 1989). However, Tsujido et al. (2015) craters are at least an order of magnitude smaller than the craters here (Tsujido et al., 2015), and astronomical craters mentioned in Melosh (1989) are orders of magnitude larger (Melosh, 1989), whereas Yamamoto et al. (2006) crater data is similar to the simulation outcomes here with a number of low-speed impact data (Yamamoto et al., 2006), hence it is believed to be more comparable with the DEM results. Moreover, a more recent study conducted on some of the craters on Bennu shows mean d_{cr}/R_{cr} as 0.2 ± 0.06, which places the results found here within the observed range with error bounds (Daly et al., 2020). Hence given this comparison, it could be concluded that the crater depths obtained here are comparable with the experimental and observational results.

Before finalizing the cratering results, it is worth noting the effect of impactor size in the results. As mentioned earlier in this chapter that the impactor-to-particle size is taken to be 5, *i.e.*, the lower boundary where the impactor size does not affect cratering results for high-speed impacts (Housen and Holsapple, 2011). In order to quantify the effect of the impactor size, three more simulations were performed with impactor radius 1, 3 and 10 cm with impactor density, $\delta = 1910$ kg/m³. The smallest these impactors has the same radius as the individual grains, thus that simulation can also be seen as impact of a grain to a granular bed. All impact speeds are 10 cm/s. With the scaling relationships derived earlier, the crater radii estimated for these impacts would be 9.3 cm, 22.4 cm, 58.7 cm. Note that the last value is larger than the simulation container size. The simulation results showed that it indeed exceeds the container size, therefore not included in the discussion here. For the smallest two impactors, Fig. 18 shows the craters that were formed in the end.

The smallest impactor only creates a depression in the surface, which would be recognized when seen from the top. The amount of ejected material is limited a few particles with a small velocities and fell back to the immediate surrounding of the crater. This result matches a recent work Bogdan et al. (2020) of low-speed grain impact to a granular bed. The authors showed that such an impact at sub-m/s speed would eject less than 10 grains (Bogdan et al., 2020), which the results here confirm. The computed crater size in this impact is 8.5 cm. This value is within ~20% of the analytically-estimated value, 9.3 cm. For 3-cm-radius impactor, the computed crater size is 22.7 cm, within 2% of the analytically-estimated value. In Housen and Holsapple (2011), it is noted that for grain size effects to vanish, the impactor has to be 5 to 10 times larger than the grains, for $U \geq 1$ km/s (Housen and Holsapple, 2011). Given the good match obtained between the analytical estimations and simulations results, it can be speculated that this value may be lower in low-velocity impacts in low gravity, *i.e.*, potentially ≤3. Even for the smallest impactor, 20% divergence from the analytical results may also be a result of the crater-size detection algorithm, as the crater appears to be slightly elliptical. A more in-depth parametric study would demonstrate the particle/impactor size effects more clearly.

5.2. Ejecta profile

5.2.1. Results

The velocity and angle of the ejected materials are discussed in this section. Recall the nondimensional velocity expression in Eq. (10). The mean velocity calculated here is normalized in the form presented in
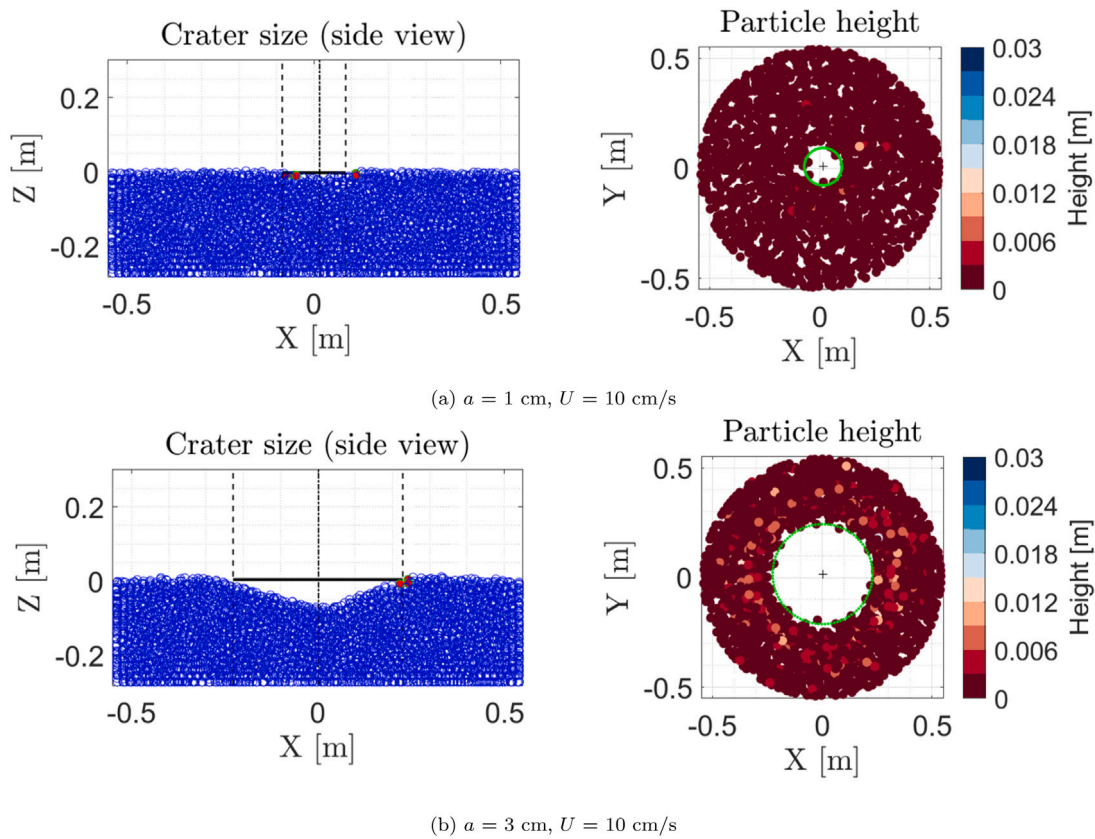
Fig. 18. Craters formed with smaller impactors. Upper left: Side view of the crater made by 1 cm radius impactor. Dashed lines and dashed dotted line denote crater boundaries and crater center, respectively. The selected particles are marked red. Upper right: Top view of the crater made by 1 cm radius impactor. First 2 cm layer of the granular bed is shown. Green circle denotes the fitted crater. Color denotes particle height from 0 cm (red) to 3 cm (blue). Lower left: Side view of the crater made by 3 cm radius impactor. Upper right: Top view of the crater made by 3 cm radius impactor. (For interpretation of the references to color in this figure legend, the reader is referred to the web version of this article.)

Eq. (10). In that case, the derived μ value is 0.56 from Table 5. Fig. 19 then shows the ejecta velocity results of all impact simulations.

According to the original crater scaling relationships and ejecta model presented by Housen and Holsapple (2011) (Fig. 2) that the ejecta model is valid between $1.2a$ and crater size R. Outside this range the relationships fails due to small ejected mass or gravity/strength effects. That region is marked approximately for the simulations here between impactor radius and crater radius. Within this range, the power law scaling appears to be valid. Beyond this range, the power-law scaling fails as in the expectations of general scaling relationships. Unlike in the case of high-speed impacts, in low-speed impacts discussed here, the failure of the power-law of scaling is also caused by irregularity in velocity of ejected material *inside* the crater bowl. This occurs when an impactor bounces off ground instead of penetrating, in which material directly underneath the impactor is mobilized but not ejected in a regular material flow but in a more stochastic manner. In the penetration case, those materials are pushed downwards and sidewards, and mobilized through streamlines even if they are to be ejected. C_1 constant defined in Eq. (10) is found between 0.2–0.6, with most of the cases clustering around 0.4.

The angle of ejection, on the other hand, has no determined value or range, but generally assumed to be constant around 45° in the literature, although observed to be decreasing radially outward from the impact point (Housen et al., 1983; Richardson et al., 2007). It is shown earlier in Figs. 9 and 10b that ejection angle is certainly not constant but varying. In order to investigate the ejection angle more generally, Fig. 20 is generated.

According to Fig. 20, majority of the ejection angle is between 40° and 60° in all simulations, and the mean value is 53°. The angle is lower for lower speed impacts and increasing with impact speed. At

the highest impact speed case, the mean angle value is placed between 55–60°, respectively. Previously, Thuillet et al. (2020) and Wada et al. (2006) also found ejection angles higher than typically assumed 45°, 48°–54° and 45°–50°, respectively. As another reference, Cintala et al. (1999) have also characterized ejection angle at ~1 km/s impacts and found varying around a mean of 45°. This study considers impacts that are a few orders of magnitude less in impact speed compared to those cited; however, this result may indicate higher ejection angle at lower impact speed. Nevertheless, it should be noted that higher ejection angles may not necessarily be a result of impact speed, but also low angle of friction (~20°) of the material used here, as noted in Housen and Holsapple (2011), which is stated to result in increased ejection velocity.

All in all, the ejecta velocity results suggest that the ejecta model developed by Housen and Holsapple (2011) for high-speed impacts may be valid for low-speed impacts as well. In the following, this relationships will be discussed more in detail in comparison with the ballistic ejecta model proposed by Richardson et al. (2007).

5.2.2. Comparison with an analytical ejecta model

The analytical ejecta model by Richardson et al. (2007), uses the ideas from Maxwell's Z-model, as discussed earlier. The model is consistent with the crater scaling relationships mathematically and its results agrees with the experiments (Richardson et al., 2007). The crater formation time plays an important role in the derivation of equations. Recall the following equation:

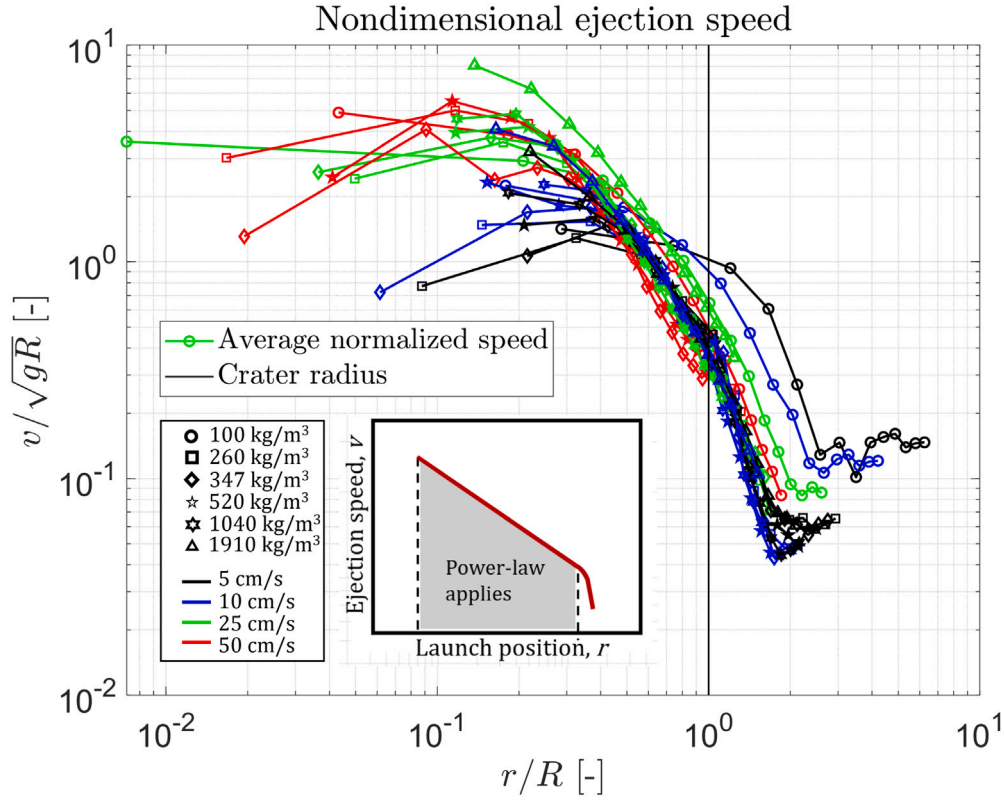$$T_g = C_{T,g}\sqrt{\frac{R_g}{g}} \tag{19}$$

Fig. 19. Average ejecta velocity profile of all simulations. The impactor radius is 5 cm. $\mu = 0.56$ is used in generating the ejecta velocity profiles. Circle (100 kg/m³), square (260 kg/m³), diamond (347 kg/m³), five-pointed star (520 kg/m³), six-pointed star (1040 kg/m³) and triangle (1910 kg/m³) represent different density values. Black, blue, green and red colors represent the impact speeds 5, 10, 25 and 50 cm/s, respectively. Vertical black line denotes crater radius, equals to 1 in normalized units. (For interpretation of the references to color in this figure legend, the reader is referred to the web version of this article.)

Eq. (19) is an approximate form of the equation where $T_g = K_{cr,g}\sqrt{\frac{V_g^3}{g}}$, where C_{T_g} is found to be $K_{cr,g} \approx C_{T_g}$ within the experimental accuracy, with the crater depth assumption as $2R_g/3$, following Melosh (1989) in high-speed cratering (Richardson et al., 2007; Melosh, 1989). Note from earlier subsections that $K_{cr,g}$ is between 0.8–0.9 (Schmidt and Housen, 1987; Melosh, 1989). However this approximation may not be true for low-speed crater under low-gravity. The cratering process takes longer under low gravity than under Earth-gravity. As shown earlier in this chapter, the depth of low-speed craters, at least in the case here, are $\sim 0.25R_g$ for the most cases. In order to find the exact value for $K_{cr,g}$, the equation $T_g = K_{cr,g}\sqrt{\frac{V_g^3}{g}}$ can be written in its full form, by assuming a paraboloid crater volume for V_g^3:

$$T_g = K_{cr,g}(\frac{\pi d}{2})^{1/3}\sqrt{\frac{R_g^{2/3}}{g}} \qquad (20)$$

where d denotes crater depth. Crater formation time is then needed to calculate $K_{cr,g}$. At this stage of the analysis, the crater time is assumed to be the time at which the *last* particle is launched from the surface. Albeit looking rather arbitrary, the post-processed data shows observationally that the last particle ejected is generally some particle that is pushed up through the very end of cratering, where downhill material movement inside the transient crater rim almost ends. Fig. 21 below shows the values of $K_{cr,g}$ as function of π_2 and time of last ejected grain, t_f.

Similar to the presentation in Schmidt and Housen (1987), t_f is presented in Fig. 21b is given as a function of $\sqrt{V^{1/3}/g}$ but in a general form given in Eq. (20). There appears two distinct cases of formation time and $K_{cr,g}$. In the first, near-constant crater formation time and as a result almost constant, clustered $K_{cr,g}$ values in Figs. 21a and 21b can

be seen. Those are mostly observed in the lowest two impact speeds and generally in lower density levels. One exception to this is a 50 cm/s impact case with 347 kg/m³ impactor. This case appears as an outlier in all simulations, like due to being in the bouncing/submerging transition density and resulting complexity during the cratering. In this first case, crater formation time is between 20 and 40 s and the $K_{cr,g}$ value is between 0.6–1.3 but mostly clustered around 1.1. In the second case, there is a linear increase in time with increasing impact speed and impactor density. The dependency to both are reasonable, as more of the impactor's momentum is given to the granular bed. The longest formation time is about 200 s, or nearly 3.5 min, while shortest is about 50 s. As a result of the long formation time, the $K_{cr,g}$ values are even higher in this case: it varies between 2.5 and 4. Note that if there were simulated impacts of 50 cm/s at impactor densities 1040 kg/m³ and 1910 kg/m³, it is highly likely that the crater formation time at those cases would be longer. Consequently, even higher $K_{cr,g}$ values may be expected.

The $K_{cr,g}$ value obtained here is close to that in Schmidt and Housen (1987) in the first case but much higher in the second. Even though the similarity in the first case is notable, it is believed that is coincidental, given the juxtaposition in the duration of the formation times in low- and high-speed impacts, as well as gravity magnitude. However, a conclusive statement on this requires further studies and potentially an alternative definition of crater formation time in the simulated impacts. The final analysis on the crater scaling relationships will be on the ejected mass in next subsection.

5.3. Ejected mass

Next, the cumulative ejected mass that travels at a velocity greater than v will be considered. Because of the intrinsic position dependence
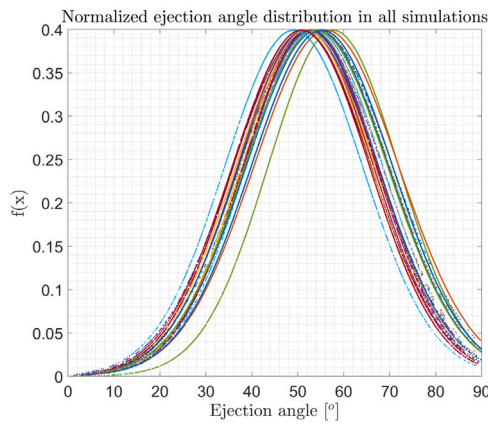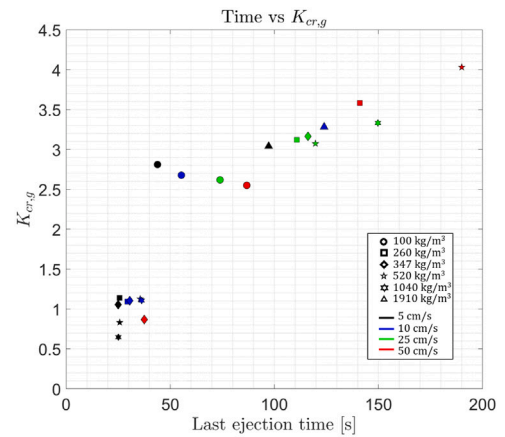
(a) Normal distribution
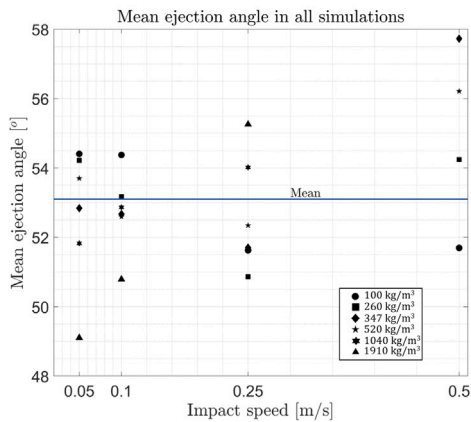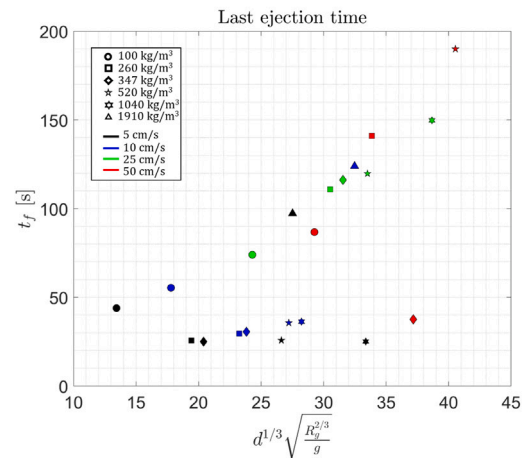

(b) Mean ejection angle

Fig. 20. Ejection angle distribution and mean angles in all presented simulations. Left: Normal distribution of ejection angles in all simulations. Right: Mean ejection angle in all simulations. Circle (100 kg/m³), square (260 kg/m³), diamond (347 kg/m³), five-pointed star (520 kg/m³), six-pointed star (1040 kg/m³) and triangle (1910 kg/m³) represent different density values. Blue line denotes the mean ejection angle calculated from all simulation data across different U and δ. Inlet shows the qualitative appearance of power-law scaling of ejected mass. (For interpretation of the references to color in this figure legend, the reader is referred to the web version of this article.)
Source: Adapted from Housen and Holsapple (2011).

(a) $K_{cr,g}$

(b) Time

Fig. 21. Last ejection time and $K_{cr,g}$ as a function of last ejection time. Left: $K_{cr,g}$ as a function of last ejection time of in an impact event. Right: Last ejection time as a function of $d^{1/3}\sqrt{\frac{R_g^{2/3}}{g}}$. In both figures, circle (100 kg/m³), square (260 kg/m³), diamond (347 kg/m³), five-pointed star (520 kg/m³), six-pointed star (1040 kg/m³) and triangle (1910 kg/m³) represent different density values. (For interpretation of the references to color in this figure legend, the reader is referred to the web version of this article.)

of v, the ejected mass is largely representative of the mass as a function of distance, even though it is not directly a function of it. However, as shown in previous sections, ejection velocity, especially in later stages of crater formation, is not always vary as a function of distance. Ejected mass is calculated with the procedure described in Section 4.2.2. The results of dimensional and nondimensional mass as defined in Eq. (11) is provided in Fig. 22.

Again, $\mu = 0.56$ for nondimensional mass profile. Ejected mass generally follows the expected ejected mass profile (Housen and Holsapple, 2011). Power-law scaling fails when close to impactor and impact point, due to little or no mass ejected, as stated by Housen and Holsapple (2011), and seen as constant line in Fig. 22. Between the end of constant region and crater size, ejected mass profile follows the power-law scaling. The ejection velocity results also appear to follow a power-law scaling until crater size (see Fig. 19). C_2 constant defined in Eq. (11) is found between 0.1–0.2 except the outliers. Moreover, almost-collapse of nondimensional ejected mass values into a single line suggest that the scaling can be achieved at low-speed and low-gravity impact regimes and impactor density dependency may be negligible.

5.4. Discussion

In the previous three subsections, different aspects of the crater-scaling relationships are collectively investigated for 5–50 cm/s impacts under small-body gravity. Those investigations are usually available individually, not together. This is enabled thanks to the opportunities provided by the quantitative nature of the DEM simulations. In terms of the crater-scaling, following remarks can be made:

- It is shown that both impactor bounce and submerge is possible during cratering, depending on the target-to-impactor density ratio. The bounce-submerge transition in this study occurs at the density ratio of 3.
- Qualitatively, it appears that the crater-scaling relationships may extend to the low-speed, low-gravity impact regimes, even though underlying physical processes are different from the high-speed impacts at kilometer-per-second level. The ejection speed and ejected mass profiles are largely similar to those presented in the earlier cratering studies (Housen and Holsapple, 2011).
- The material-dependent scaling-coefficient μ, which relates energy or momentum of the impactor to crater size, is found 0.56,
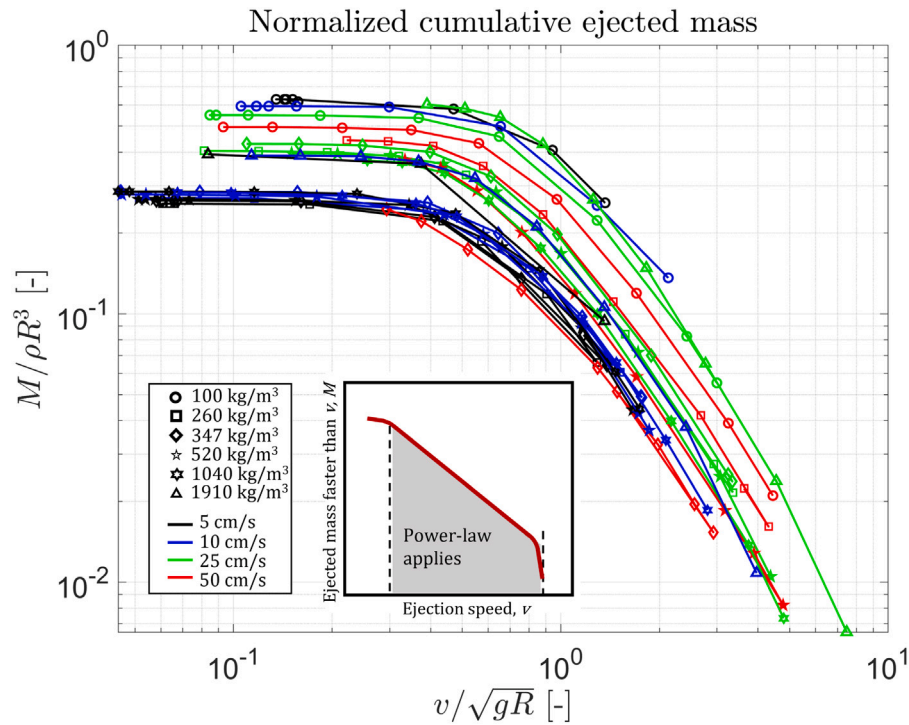
Fig. 22. Ejected mass as a function of average ejecta velocity. $\mu = 0.56$ is used. Circle (100 kg/m³), square (260 kg/m³), diamond (347 kg/m³), five-pointed star (520 kg/m³), six-pointed star (1040 kg/m³) and triangle (1910 kg/m³) represent different density values. Black, blue, green and red colors represent the impact speeds 5, 10, 25 and 50 cm/s, respectively. Inlet shows the qualitative appearance of power-law scaling of ejected mass. (For interpretation of the references to color in this figure legend, the reader is referred to the web version of this article.)

a value consistent with the expectation of the crater scaling relationships. The density effects on this value appear to be negligible, even though further studies are necessary to assess this conclusion. The μ value typically found as ~0.40 in Earth-based impact studies. Previous studies also showed values ~0.55 for impacts on water (Housen and Holsapple, 2011). It is observed in the experimental studies that the impacts in glass-bead-type materials result in exaggerated craters and higher ejection speeds (Housen and Holsapple, 2011). Combined with lower gravity, the glass-bead type material used in this study may have resulted in the obtained coefficient.

- The crater radius scales with impact energy as $R_{cr} = 1.014 \times E_{imp}^{0.217}$.
- The crater depth scales with the crater radius as $d_{cr} \sim 0.25 R_{cr}$
- The long crater formation observed in the SCI experiment of the Hayabusa2 mission is also observed here, despite much lower impact speeds. The formation time, calculated as the time of the last grain ejection, is about 200 s, or about 3.5 min, at the longest case. This is much higher than the crater formation times on Earth at the same impact conditions, hence once again underscores the difficulty of testing low-speed cratering under Earth-based conditions. Consequently, the relevant scaling coefficient, here denoted as $K_{cr,g}$ is shown to have two different regimes related to bouncing and submerging. $K_{cr,g}$ value related to bouncing is computed approximately 1. On the other hand, $K_{cr,g}$ value related to submerging is found between 2.5 and 4. Recall that the previous high-speed impact experiments on Earth presented values between 0.8 and 0.9 (Schmidt and Housen, 1987; Melosh, 1989).

After providing a summary of the results, it is now reasonable to compare the simulation results in the general picture of the previous studies, as presented in Fig. 3. The π-scaling results from the simulations are added to Fig. 3 and presented Fig. 23.

The theory lines are generated with impact and target parameters of Takizawa and Katsuragi (2020) and with generic parameters K_1

= 1.03, ν = 0.4 and μ = 0.41 from Holsapple and Housen (2007). The most of the simulation results appear to be slightly outside of the bounds. This is to be expected, however: As noted earlier, low angle-of-friction of the selected DEM parameters result in larger craters (Housen and Holsapple, 2011), which eventually increase the normalized crater value. Impact simulations with more frictional materials would likely to result in smaller craters, therefore reduce the offset between the simulations and experimental studies.

All in all, the original results presented here provides a strong case in favor of the applicability of the crater-scaling relationships for low-speed impacts under low-gravity. It is clear that more data is necessary to constrain the parameters, particularly μ and ν in order to build a more robust crater scaling relationships in this impact regime.

The results presented throughout the paper have implications on the evolution of small-bodies as well. In geological time scales, material escaped in low-speed impacts, which may now be estimated through the scaling relationships presented here, may alter the size, rotation period, and orbit of the body (Scheeres et al., 2019). Even though it is not discussed in this study, oblique impacts must be much more frequent than near-normal impact discussed here, hence the asymmetry in the material ejection may further alter the rotation period and direction. Even if little or no material is lost in low-speed impacts, fallen-back material after brief orbital motions, would slowly but constantly alter a small-body's surface, covering one part of the body while exposing the other. This would also potentially complicate understanding the space-weathering process. Therefore, it appears that, while large-scale events such as collisions make abrupt and more distinguishable changes in a small-body, smaller scale events such as low-speed impacts as presented here would result in a more subtle but continuous alteration processes. It is likely that the future small-body missions will provide better understanding on the evolution of small-bodies.

Finally, the result obtained here could also be useful for small-body surface exploration missions. If a spacecraft landing is of interest, the power-law relationships derived for crater sizes, ejecta properties and formation time can be used for safeguarding measures during
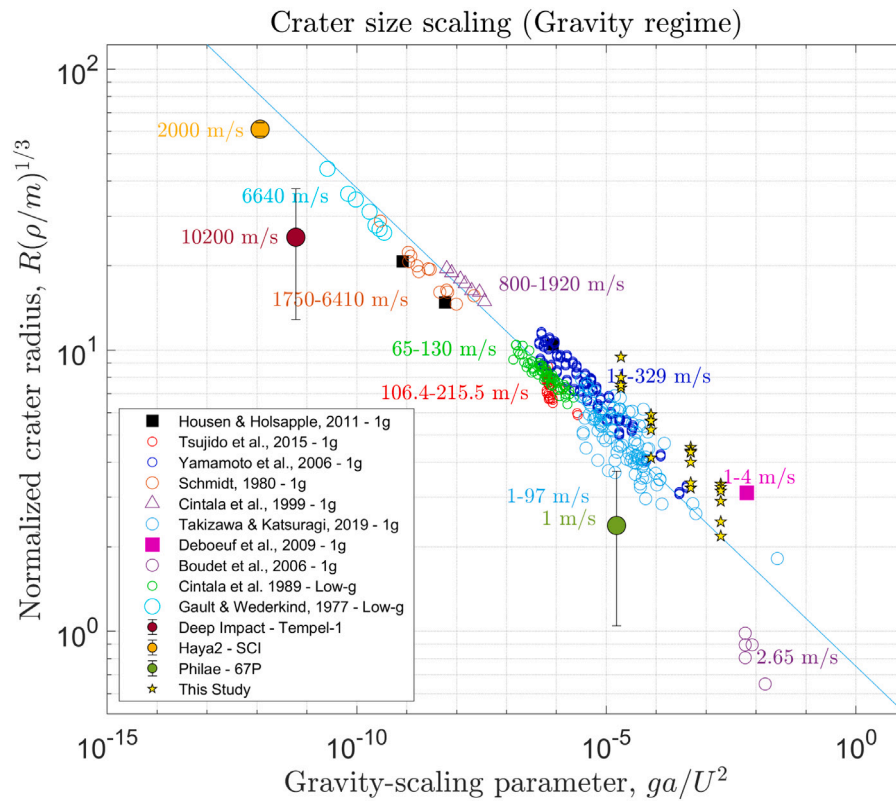
Fig. 23. Previous experimental studies with the simulation results presented here. Gold five-pointed stars denote values found in this study. (For interpretation of the references to color in this figure legend, the reader is referred to the web version of this article.)

landing operations. For example, a degradation is reported in one of the cameras of Hayabusa2 during the sampling operations (Kouyama et al., 2021). In order to avoid such situations, a spacecraft engineer can use the estimated mass, ejection angle and speed by the crater-scaling relationships to estimate the risk involved to spacecraft instruments (particularly those facing the surface) from ejected particles during surface interaction and after take-off. With given mass of spacecraft and approximate landing pad area, first-order approximations can be made with spherical impactor assumption. It is clear that spacecraft are generally non-homogeneous and often with non-spherical landing pads. The crater-scaling relationships derived here assumes the point-source approximation through the coupling parameter C. It means that a can be taken as the radius of an approximated sphere of the interacting landing pad surface with the mass of spacecraft. If there are multiple landing pads, the mass should be distributed to each pad, under the assumption that all landing pads will touch the surface at the same time. This treatment of the problem means that impactor density δ will be different for spacecraft and impactors. The current and previous studies could not clearly demonstrate the δ dependency on crater scaling, at least in lower speed impacts, or have rather shown a weak dependency. Therefore, the δ dependency may need to be explored further, as δ can be large for a spacecraft interacting with the surface of a small body. Moreover, for a more accurate scaling of craters and their ejecta, it is necessary to perform dedicated simulations at the later stages of design process. That is because crater shapes and sizes, as well as corresponding ejecta properties would potentially differ with non-spherical landing pads, or samplers with landing pad like structure. Moreover, for more harpoon-like penetrators, or in the cases where force applied or experienced by spacecraft are important, it may be appropriate to use dedicated granular force models for small body surfaces (Ballouz et al., 2021).

6. Conclusions

The applicability of the crater-scaling relationships to low-speed impact cratering under low-gravity is of interest in order to understand surface mechanical properties of small-bodies, to reveal their incessant evolution over their lifetime and to make informed decisions during the surface operation of the small-body exploration missions. The current low-gravity platforms available on Earth lack the level and duration of low gravity, or the access to and controllability in experiments, as well as the sufficient quantitative measurements to test the different aspects of cratering in this regime. In order to overcome these limitations, and provide quantitative insights into the applicability of crater scaling relationships in low-speed impacts under low gravity, a discrete-element method (DEM) based numerical simulation approach is employed. While the application of the DEM simulations to low-speed impacts for low-gravity applications is not novel, the proposed systematic post-processing procedure and its application to test the crater-scaling relationships in centimeter-per-level impacts under microgravity conditions are first to the best of authors' knowledge.

The research first builds a case on the potential applicability of the long-established crater scaling relationships by collectively investigating the previous crater size scaling results from the experiments and the space missions. The investigated crater sizes demonstrate scaling across five orders of magnitude of impact speeds. This suggests that even though the underlying physical process can be different between kilometer-per-second and centimeter-per-second speed impacts, the fundamental dependencies to macro parameters (e.g., gravity and bulk density among the others) may be similar. Building on this hypothesis, a set of DEM simulations is performed by varying impactor density and impact speed from the frequently encountered values on small-body surfaces. A systematic procedure is presented to post-process the obtained data, particularly for crater sizes but also for ejection velocity, angle, ejected mass, and the formation time. Qualitatively, the

Table A.6

Tabulated simulation conditions and outcomes. All simulations under 9.80665e−5 m/s^2 (0.00001 g). Radius of all impactors is 0.05 m. S: Submerge. B: Bounce.

#	U [m/s]	δ [m³]	ρ [m³]	DEM ParSet	R_{cr}[m]	d_{cr}[m]	π_2	π_R	Out
1	0.05	100	975.4	GB	0.0806	0.0292	2.000e−3	2.1815	B
2	0.10	100	975.4	GB	0.1195	0.0458	4.903e−4	3.2354	B
3	0.25	100	975.4	GB	0.1923	0.0725	7.845e−5	5.2086	B
4	0.50	100	975.4	GB	0.2711	0.0898	1.961e−5	7.3425	B
5	0.05	260	975.4	GB	0.1697	0.0420	2.000e−3	3.3428	B
6	0.10	260	975.4	GB	0.2292	0.0533	4.903e−4	4.5133	B
7	0.25	260	975.4	GB	0.2995	0.0922	7.845e−5	5.8987	B
8	0.50	260	975.4	GB	0.3818	0.0987	1.961e−5	7.5201	B
9	0.05	347	975.4	GB	0.1819	0.0453	2.000e−3	3.2538	B
10	0.10	347	975.4	GB	0.2448	0.0536	4.903e−4	4.3791	B
11	0.25	347	975.4	GB	0.3122	0.0977	7.845e−5	5.5848	B
12	0.50	347	975.4	GB	0.5290	0.0943	1.961e−5	9.4622	B
13	0.05	520	975.4	GB	0.2019	0.0907	2.000e−3	3.1568	S
14	0.10	520	975.4	GB	0.2774	0.0706	4.903e−4	4.3365	S
15	0.25	520	975.4	GB	0.3585	0.1019	7.845e−5	5.6035	S
16	0.50	520	975.4	GB	0.5119	0.1264	1.961e−5	8.0022	S
17	0.05	1040	975.4	GB	0.2340	0.1543	2.000e−3	2.9027	S
18	0.10	1040	975.4	GB	0.3219	0.0679	4.903e−4	3.9937	S
19	0.25	1040	975.4	GB	0.4519	0.1242	7.845e−5	5.6071	S
20	0.05	1910	975.4	GB	0.2422	0.0836	2.000e−3	2.4537	S
21	0.10	1910	975.4	GB	0.3331	0.0999	4.903e−4	3.3748	S
22	0.25	1910	975.4	GB	0.4086	0.2388	7.845e−5	4.1398	S

cases of both impactor bounce and submerge were observed, unlike of the Earth-based experiments. By using the quantitative opportunities provided by the DEM simulations, the standard scaling coefficients of the crater scaling relationships are obtained, the profiles of ejection velocities, the total amount of ejected material is calculated, and a statistical distribution of ejection angle is presented. The expected scaling profiles from the crater-scaling relationships are validated. The final scaling shows slightly higher values than those usually encountered on Earth-based experiments. All in all, however, the study demonstrates the potential applicability of the relationships for the impact regimes considered here. The presented results will be useful to shed light on the speculated low-speed craters on and material loss from small-bodies, as well inform landing and proximity operations of the future small-body exploration missions.

It appears clear that further simulations are needed to understand the cratering process and the scaling relationships in this impact regime, constrain the scaling coefficients with the DEM parameters specifically tailored for materials and the impact conditions of interest. Until then, a cautious approach may be necessary before applying these results to a wider cases of interest. For different impact conditions of interest further improvements in the post-processing algorithm may be necessary to account for a variety of crater shapes that may appear at the end of an impact. Finally, the current drawbacks of the DEM simulations, e.g. the trade-off between particle size and simulation duration or container size, would likely be alleviated with the advancement of computational techniques and increase in the computational power.

Acknowledgments

Appendix A. Impact simulation results

See Table A.6.

References

Arakawa, M., Saiki, T., Wada, K., Ogawa, K., Kadono, T., Shirai, K., Sawada, H., Ishibashi, K., Honda, R., Sakatani, N., Iijima, Y., Okamoto, C., Yano, H., Takagi, Y., Hayakawa, M., Michel, P., Jutzi, M., Shimaki, Y., Kimura, S., Mimasu, Y., Toda, T., Imamura, H., Nakazawa, S., Hayakawa, H., Sugita, S., Morota, T., Kameda, S., Tatsumi, E., Cho, Y., Yoshioka, K., Yokota, Y., Matsuoka, M., Yamada, M., Kouyama, T., Honda, C., Tsuda, Y., Watanabe, S., Yoshikawa, M., Tanaka, S., Terui, F., Kikuchi, S., Yamaguchi, T., Ogawa, N., Ono, G., Yoshikawa, K., Takahashi, T., Takei, Y., Fujii, A., Takeuchi, H., Yamamoto, Y., Okada, T., Hirose, C., Hosoda, S., Mori, O., Shimada, T., Soldini, S., Tsukizaki, R., Iwata, T., Ozaki, M., Abe, M., Namiki, N., Kitazato, K., Tachibana, S., Ikeda, H., Hirata, N., Hirata, N., Noguchi, R., Miura, A., 2020. An artificial impact on the asteroid 162173 ryugu formed a crater in the gravity-dominated regime. Science 1701 (March), http://dx.doi.org/10.1126/science.aaz1701.

Ballouz, R., 2017. Numerical Simulations of Granular Physics in the Solar System (Ph.D. thesis). University of Maryland, College Park.

Ballouz, R.L., Richardson, D.C., Michel, P., Schwartz, S.R., Yu, Y., 2015. Numerical simulations of collisional disruption of rotating gravitational aggregates: Dependence on material properties. Planet. Space Sci. 107 (1), 29–35. http://dx.doi.org/10.1016/j.pss.2014.06.003.

Ballouz, R.-L., Walsh, K.J., Richardson, D.C., Michel, P., 2019. Using a geometrical algorithm to provide N-body initial conditions for the gravitational phase of asteroid family formation. Mon. Not. R. Astron. Soc. 485 (1), 697–707. http://dx.doi.org/10.1093/mnras/stz410.

Ballouz, R.-L., Walsh, K.J., Sánchez, P., Holsapple, K.A., Michel, P., Scheeres, D.J., Zhang, Y., Richardson, D.C., Barnouin, O.S., Nolan, M.C., Bierhaus, E.B., Connolly, J., Schwartz, S.R., Çelik, O., Baba, M., Lauretta, D.S., 2021. Modified granular impact force laws for the OSIRIS-REx touchdown on the surface of asteroid (101955) bennu. Mon. Not. R. Astron. Soc. 507 (4), 5087–5105. http://dx.doi.org/10.1093/mnras/stab2365.

Barnouin, O.S., Daly, M.G., Palmer, E.E., Gaskell, R.W., Weirich, J.R., Johnson, C.L., Al Asad, M.M., Roberts, J.H., Perry, M.E., Susorney, H.C.M., Daly, R.T., Bierhaus, E.B., Seabrook, J.A., Espiritu, R.C., Nair, A.H., Nguyen, L., Neumann, G.A., Ernst, C.M., Boynton, W.V., Nolan, M.C., Adam, C.D., Moreau, M.C., Rizk, B., Drouet D'Aubigny, C.Y., Jawin, E.R., Walsh, K.J., Michel, P., Schwartz, S.R., Ballouz, R.-L., Mazarico, E.M., Scheeres, D.J., McMahon, J.W., Bottke, W.F., Sugita, S., Hirata, N., Hirata, N., Watanabe, S.-i., Burke, K.N., DellaGiustina, D.N., Bennett, C.A., Lauretta, D.S., 2019. Shape of (101955) bennu indicative of a rubble pile with internal stiffness. Nat. Geosci. 12 (4), 247–252. http://dx.doi.org/10.1038/s41561-019-0330-x.

Biele, J., Ulamec, S., Maibaum, M., Roll, R., Witte, L., Jurado, E., Munoz, P., Arnold, W., Auster, H.-U., Casas, C., Faber, C., Fantinati, C., Finke, F., Fischer, H.-H., Geurts, K., Guttler, C., Heinisch, P., Herique, A., Hviid, S., Kargl, G., Knapmeyer, M., Knollenberg, J., Kofman, W., Komle, N., Kuhrt, E., Lommatsch, V., Mottola, S., Pardo de Santayana, R., Remetean, E., Scholten, F., Seidensticker, K.J., Sierks, H., Spohn, T., 2015. The landing(s) of philae and inferences about comet surface mechanical properties. Science 349 (6247), 1–6. http://dx.doi.org/10.1126/science.aaa9816.

Bogdan, T., Kollmer, J.E., Teiser, J., Kruss, M., Wurm, G., 2020. Laboratory impact splash experiments to simulate asteroid surfaces. Icarus 341 (113646), http://dx.doi.org/10.1016/j.icarus.2020.113646.

Bottke, W.F., Moorhead, A.V., Connolly, H.C., Hergenrother, C.W., Molaro, J.L., Michel, P., Nolan, M.C., Schwartz, S.R., Vokrouhlický, D., Walsh, K.J., Lauretta, D.S., 2020. Meteoroid impacts as a source of bennu's particle ejection events. J. Geophys. Res.: Planets 125 (8), http://dx.doi.org/10.1029/2019JE006282.

Boudet, J.F., Amarouchene, Y., Kellay, H., 2006. Dynamics of impact cratering in shallow sand layers. Phys. Rev. Lett. 96 (15), 1–4. http://dx.doi.org/10.1103/PhysRevLett.96.158001.

Brisset, J., Colwell, J., Dove, A., Abukhalil, S., Cox, C., Mohammed, N., 2018. Regolith behavior under asteroid-level gravity conditions: low-velocity impact experiments. Prog. Earth Planet. Sci. 5 (1), 73. http://dx.doi.org/10.1186/s40645-018-0222-5.

Brownlee, D.E., Horz, F., Newburn, R.L., Zolensky, M., Duxbury, T.C., Sandford, S., Sekanina, Z., Tsou, P., Hanner, M.S., Clark, B.C., et al., 2004. Surface of young jupiter family comet 81p/wild 2: View from the stardust spacecraft. Science 304 (5678), 1764–1769. http://dx.doi.org/10.1126/science.1097899.

Buckingham, E., 1914. On physically similar systems; illustrations of the use of dimensional equations. Phys. Rev. 4 (4), 345. http://dx.doi.org/10.1103/PhysRev.4.345.

Burke, K.N., DellaGiustina, D.N., Bennett, C.A., Walsh, K.J., Pajola, M., Bierhaus, E.B., Nolan, M.C., Boynton, W.V., Brodbeck, J.I., Connolly, H.C., Prasanna Deshapriya, J.D., Dworkin, J.P., Elder, C.M., Golish, D.R., Hoover, R.H., Jawin, E.R., McCoy, T.J., Michel, P., Molaro, J.L., Nolau, J.O., Padilla, J., Rizk, B., Robbins, S.J., Sahr, E.M., Smith, P.H., Stewart, S.J., Susorney, H.C.M., Enos, H.L., Lauretta, D.S., 2021. Particle size-frequency distributions of the OSIRIS-REx candidate sample sites on asteroid (101955) bennu. Remote Sens. 13 (7), 1315. http://dx.doi.org/10.3390/rs13071315.

Çelik, O., 2020. Object-Surface Interaction in Small-Body Surfaces (Ph.D. thesis). The Graduate University for Advanced Studies, SOKENDAI, Sagamihara, Japan.

Çelik, O., Baresi, N., Ballouz, R.-L., Ogawa, K., Wada, K., Kawakatsu, Y., 2019. Ballistic deployment from quasi-satellite orbits around phobos under realistic dynamical and surface environment constraints. Planet. Space Sci. 178 (104693), http://dx.doi.org/10.1016/j.pss.2019.06.010.

Cheng, B., Yu, Y., Baoyin, H., 2019. Numerical simulations of the controlled motion of a hopping asteroid lander on the regolith surface. Mon. Not. R. Astron. Soc. 485 (3), 3097–3111. http://dx.doi.org/10.1093/mnras/stz633.

Chesley, S.R., French, A.S., Davis, A.B., Jacobson, R.A., Brozović, M., Farnocchia, D., Selznick, S., Liounis, A.J., Hergenrother, C.W., Moreau, M.C., Pelgrift, J., Lessac-Chenen, E., Molaro, J.L., Park, R.S., Rozitis, B., Scheeres, D.J., Takahashi, Y., Vokrouhlický, D., Wolner, C.W.V., Adam, C., Bos, B.J., Christensen, E.J., Emery, J.P., Leonard, J.M., McMahon, J.W., Nolan, M.C., Shelly, F.C., Lauretta, D.S., 2020. Trajectory estimation for particles observed in the vicinity of (101955) bennu. J. Geophys. Res.: Planets 125 (9), http://dx.doi.org/10.1029/2019JE006363.

Cintala, M.J., Berthoud, L., Hörz, F., 1999. Ejection-velocity distributions from impacts into coarse-grained sand. Meteorit. Planet. Sci. 34 (4), 605–623. http://dx.doi.org/10.1111/j.1945-5100.1999.tb01367.x.

Cintala, M.J., Horz, F., See, T.H., 1989. Impact cratering in low-gravity enviornments: Results of reconnaissance experimentation on the NASA KC-135a reduced gravity aircraft. In: 19th Lunar and Planetary Science Conference. pp. 627–639.

Colwell, J.E., 2003. Low velocity impacts into dust: Results from the COLLIDE-2 microgravity experiment. Icarus 164 (1), 188–196. http://dx.doi.org/10.1016/S0019-1035(03)00083-6.

Colwell, J.E., Sture, S., Cintala, M., Durda, D., Hendrix, A., Goudie, T., Curtis, D., Ashcom, D.J., Kanter, M., Keohane, T., Lemos, A., Lupton, M., Route, M., 2008. Ejecta from impacts at 0.2–2.3 m/s in low gravity. Icarus 195 (2), 908–917. http://dx.doi.org/10.1016/j.icarus.2007.12.019.

Colwell, J.E., Taylor, M., 1999. Low-velocity microgravity impact experiments into simulated regolith, Vol. 138, (2), pp. 241–248. http://dx.doi.org/10.1006/icar.1998.6073.

Daly, R.T., Bierhaus, E.B., Barnouin, O.S., Daly, M.G., Seabrook, J.A., Roberts, J.H., Ernst, C.M., Perry, M.E., Nair, H., Espiritu, R.C., Palmer, E.E., Gaskell, R.W., Weirich, J.R., Susorney, H.C.M., Johnson, C.L., Walsh, K.J., Nolan, M.C., Jawin, E.R., Michel, P., Trang, D., Lauretta, D.S., 2020. The morphometry of impact craters on bennu. Geophys. Res. Lett. 47 (24), e2020GL089672. http://dx.doi.org/10.1029/2020GL089672.

Daniels, K.E., 2013. Rubble-pile near earth objects: insights from granular physics. In: Asteroids. Springer, pp. 271–286.

De Vet, S.J., De Bruyn, J.R., 2007. Shape of impact craters in granular media. Phys. Rev. E 76 (4), 1–6. http://dx.doi.org/10.1103/PhysRevE.76.041306.

Debœuf, S., Gondret, P., Rabaud, M., 2009. Dynamics of grain ejection by sphere impact on a granular bed. Phys. Rev. E 79 (4), 1–9. http://dx.doi.org/10.1103/PhysRevE.79.041306.

Durda, D.D., Chapman, C.R., Merline, W.J., Enke, B.L., 2012. Detecting crater ejecta-blanket boundaries and constraining source crater regions for boulder tracks and elongated secondary craters on eros. Meteorit. Planet. Sci. 47 (6), 1087–1097.

Edelsbrunner, H., Mücke, E.P., 1994. Three-dimensional alpha shapes. ACM Trans. Graph. 13 (1), 43–72. http://dx.doi.org/10.1145/174462.156635.

Gault, D.E., Wedekind, J.A., 1977. Experimental hypervelocity impact into quartz sand - II, effects of gravitational acceleration. In: Impact and Explosion Cratering. Pergamon, New York, NY, pp. 1231–1244.

Geissler, P., Petit, J.-M., Durda, D.D., Greenberg, R., Bottke, W., Nolan, M., Moore, J., 1996. Erosion and ejecta reaccretion on 243 ida and its moon. Icarus 120 (1), 140–157. http://dx.doi.org/10.1006/icar.1996.0042.

Hayashi, K., Sumita, I., 2017. Low-velocity impact cratering experiments in granular slopes. Icarus 291, 160–175. http://dx.doi.org/10.1016/j.icarus.2017.03.027.

Hergenrother, C.W., Adam, C.D., Chesley, S.R., Lauretta, D.S., 2020. Introduction to the special issue: Exploration of the activity of asteroid (101955) bennu. J. Geophys. Res.: Planets 125 (9), 1–15. http://dx.doi.org/10.1029/2020JE006549.

Holsapple, K.A., 1993. The scaling of impact processes in planetary sciences. Annu. Rev. Earth Planet. Sci. 21 (1), 333–373.

Holsapple, K.A., Housen, K.R., 2007. A crater and its ejecta: An interpretation of deep impact. Icarus 191, 586–597. http://dx.doi.org/10.1016/j.icarus.2006.08.035.

Holsapple, K., Schmidt, R., 1982. On the scaling of crater dimensions: 2. Impact processes. J. Geophys. Res.: Solid Earth 87 (B3), 1849–1870. http://dx.doi.org/10.1029/JB087iB03p01849.

Housen, K.R., Holsapple, K.A., 2011. Ejecta from impact craters. Icarus 211 (1), 856–875. http://dx.doi.org/10.1016/j.icarus.2010.09.017.

Housen, K., Schmidt, R., Holsapple, K., 1983. Crater ejecta scaling laws: Fundamental forms based on dimensional analysis. J. Geophys. Res.: Solid Earth 88 (B3), 2485–2499. http://dx.doi.org/10.1029/JB088iB03p02485.

Joeris, K., Schönau, L., Schmidt, L., Keulen, M., Desai, V., Born, P., Kollmer, J.E., 2021. Experiments on rebounding slow impacts under asteroid conditions. In: EPJ Web of Conferences, Vol. 249. EDP Sciences, p. 13003. http://dx.doi.org/10.1051/epjconf/202124913003.

Kiuchi, M., Nakamura, A.M., Wada, K., 2019. Experimental study on gravitational and atmospheric effects on crater size formed by low-velocity impacts into granular media. J. Geophys. Res.: Planets 124 (5), 1379–1392. http://dx.doi.org/10.1029/2018JE005628.

Kouyama, T., Tatsumi, E., Yokota, Y., Yumoto, K., Yamada, M., Honda, R., Kameda, S., Suzuki, H., Sakatani, N., Hayakawa, M., et al., 2021. Post-arrival calibration of hayabusa2's optical navigation cameras (ONCs): Severe effects from touchdown events. Icarus 360, 114353. http://dx.doi.org/10.1016/j.icarus.2021.114353.

Kuzmin, R., Shingareva, T., Zabalueva, E., 2003. An engineering model for the phobos surface. Sol. Syst. Res. 37 (4), 266–281. http://dx.doi.org/10.1023/A:1025074114117.

Lauretta, D., Hergenrother, C., Chesley, S., Leonard, J., Pelgrift, J., Adam, C., Al Asad, M., Antreasian, P., Ballouz, R.-L., Becker, K., et al., 2019. Episodes of particle ejection from the surface of the active asteroid (101955) bennu. Science 366 (6470), http://dx.doi.org/10.1126/science.aay3544.

Lauretta, D.S., OSIRIS-REx TAG Team, 2021. The OSIRIS-REx touch-and-go sample acquisition event and implications for the nature of the returned sample. In: Lunar and Planetary Science Conference.

Maurel, C., Michel, P., Biele, J., Ballouz, R.-L., Thuillet, F., 2018. Numerical simulations of the contact between the lander MASCOT and a regolith-covered surface. Adv. Space Res. 62 (8), 2099–2124. http://dx.doi.org/10.1016/j.asr.2017.05.029.

Melosh, H.J., 1989. Impact Cratering: A Geologic Process. Oxford University Press.

Michel, P., Schwartz, S.R., Richardson, D.C., Machii, N., Nakamura, A.M., 2011. Simulations of low-speed impacts into cohesive aggregates and comparison with experiments on sintered glass bead agglomerates. In: European Planetary Science Conference, Vol. 6.

Miyamoto, H., Yano, H., Scheeres, D.J., Abe, S., Barnouin-Jha, O., Cheng, A.F., Demura, H., Gaskell, R.W., Hirata, N., Ishiguro, M., et al., 2007. Regolith migration and sorting on asteroid itokawa. Science 316 (5827), 1011–1014. http://dx.doi.org/10.1126/science.1134390.

Mottola, S., Arnold, G., Grothues, H.-G., Jaumann, R., Michaelis, H., Neukum, G., Bibring, J.-P., Schröder, S., Hamm, M., Otto, K., et al., 2015. The structure of the regolith on 67p/churyumov-gerasimenko from rolis descent imaging. Science 349 (6247), http://dx.doi.org/10.1126/science.aab0232.

Murdoch, N., Drilleau, M., Sunday, C., Thuillet, F., Wilhelm, A., Nguyen, G., Gourinat, Y., 2021. Low-velocity impacts into granular material: application to small-body landing. Mon. Not. R. Astron. Soc. http://dx.doi.org/10.1093/mnras/stab624.

Pelgrift, J.Y., Lessac-Chenen, E.J., Adam, C.D., Leonard, J.M., Nelson, D.S., McCarthy, L., Sahr, E.M., Liounis, A., Moreau, M., Bos, B.J., Hergenrother, C.W., Lauretta, D.S., 2020. Reconstruction of bennu particle events from sparse data. Earth Space Sci. 7 (8), e2019EA000938. http://dx.doi.org/10.1029/2019EA000938.

Richardson, D.C., Blum, J., Weinhart, T., Schwartz, S.R., Michel, P., Walsh, K.J., 2012. Numerical simulations of landslides calibrated against laboratory experiments for application to asteroid surface processes. In: AAS/Division for Planetary Sciences Meeting Abstracts #44.

Richardson, J.E., Melosh, H.J., 2013. An examination of the deep impact collision site on comet tempel 1 via stardust-next: Placing further constraints on cometary surface properties. Icarus 222 (2), 492–501. http://dx.doi.org/10.1016/j.icarus.2012.04.019.

Richardson, J.E., Melosh, H.J., Lisse, C.M., Carcich, B., 2007. A ballistics analysis of the deep impact ejecta plume: Determining comet tempel 1's gravity, mass, and density. Icarus 191, 176–209. http://dx.doi.org/10.1016/j.icarus.2007.08.033.

Sánchez, P., Scheeres, D.J., 2011. Simulating asteroid rubble piles with a self-gravitating soft-sphere distinct element method model. Astrophys. J. 727 (2), 120. http://dx.doi.org/10.1088/0004-637X/727/2/120.

Sawada, H., Ogawa, K., Shirai, K., Kimura, S., Hiromori, Y., Mimasu, Y., 2017. Deployable camera (DCAM3) system for observation of Hayabusa2 impact experiment. Space Sci. Rev. 208, 143–164. http://dx.doi.org/10.1007/s11214-017-0337-9.

Scheeres, D.J., Hartzell, C.M., Sánchez, P., Swift, M., 2010. Scaling forces to asteroid surfaces: The role of cohesion. Icarus 210 (2), 968–984. http://dx.doi.org/10.1016/j.icarus.2010.07.009.

Scheeres, D.J., McMahon, J.W., French, A.S., Brack, D.N., Chesley, S.R., Farnocchia, D., Takahashi, Y., Leonard, J.M., Geeraert, J., Page, B., Antreasian, P., Getzandanner, K., Rowlands, D., Mazarico, E.M., Small, J., Highsmith, D.E., Moreau, M., Emery, J.P., Rozitis, B., Hirabayashi, M., Sánchez, P., Van wal, S., Tricarico, P., Ballouz, R.L., et al., 2019. The dynamic geophysical environment of (101955) bennu based on OSIRIS-REx measurements. Nat. Astron. 3 (4), 352–361. http://dx.doi.org/10.1038/s41550-019-0721-3.

Schmidt, R., 1980. Meteor crater: energy of formation-implications of centrifuge scaling. In: 11th Lunar and Planetary Science Conference. pp. 2099–2128.

Schmidt, R.M., Housen, K.R., 1987. Some recent advances in the scaling of impact and explosion cratering. Int. J. Impact Eng. 5 (1–4), 543–560. http://dx.doi.org/10.1016/0734-743X(87)90069-8.

Scholten, F., Preusker, F., Elgner, S., Matz, K.-D., Jaumann, R., Biele, J., Hercik, D., Auster, H.-U., Hamm, M., Grott, M., Grimm, C., Ho, T.-M., Koncz, A., Schmitz, N., Trauthan, F., Kameda, S., Sugita, S., Honda, R., Morota, T., Tatsumi, E., Cho, Y., Yoshioka, K., Sawada, H., Yokota, Y., Sakatani, N., Hayakawa, M., Matsuoka, M., Yamada, M., Kouyama, T., Suzuki, H., Honda, C., Ogawa, K., 2019. The descent and bouncing path of the Hayabusa2 lander MASCOT at asteroid (162173) ryugu. Astron. Astrophys. 632, L3. http://dx.doi.org/10.1051/0004-6361/201936757.

Schwartz, S.R., Michel, P., Richardson, D.C., Yano, H., 2014. Low-speed impact simulations into regolith in support of asteroid sampling mechanism design I: Comparison with 1-g experiments. Planet. Space Sci. 103, 174–183. http://dx.doi.org/10.1016/j.pss.2014.07.013.

Schwartz, S.R., Richardson, D.C., Michel, P., 2012. An implementation of the soft-sphere discrete element method in a high-performance parallel gravity tree-code. Granul. Matter 14 (3), 363–380. http://dx.doi.org/10.1007/s10035-012-0346-z.

Seguin, A., Bertho, Y., Gondret, P., 2008. Influence of confinement on granular penetration by impact. Phys. Rev. E 78 (1), http://dx.doi.org/10.1103/PhysRevE.78.010301.

Sugita, S., Honda, R., Morota, T., Kameda, S., Sawada, H., Tatsumi, E., Yamada, M., Honda, C., Yokota, Y., Kouyama, T., Sakatani, N., Ogawa, K., Suzuki, H., Okada, T., Namiki, N., Tanaka, S., Iijima, Y., Yoshioka, K., Hayakawa, M., Cho, Y., Matsuoka, M., Hirata, N., Hirata, N., Miyamoto, H., Domingue, D., Hirabayashi, M., Nakamura, T., Hiroi, T., Michikami, T., Michel, P., Ballouz, R.L., Barnouin, O.S., Ernst, C.M., Schröder, S.E., Kikuchi, H., Hemmi, R., Komatsu, G., Fukuhara, T., Taguchi, M., Arai, T., Senshu, H., Demura, H., Ogawa, Y., Shimaki, Y., Sekiguchi, T., Müller, T.G., Hagermann, A., Mizuno, T., Noda, H., Matsumoto, K., Yamada, R., Ishihara, Y., Ikeda, H., Araki, H., Yamamoto, K., Abe, S., Yoshida, F., Higuchi, A., Sasaki, S., Oshigami, S., Tsuruta, S., Asari, K., Tazawa, S., Shizugami, M., Kimura, J., Otsubo, T., Yabuta, H., Hasegawa, S., Ishiguro, M., Tachibana, S., Palmer, E., Gaskell, R., Le Corre, L., Jaumann, R., Otto, K., Schmitz, N., Abell, P.A., Barucci, M.A., Zolensky, M.E., Vilas, F., Thuillet, F., Sugimoto, C., Takaki, N., Suzuki, Y., Kamiyoshihara, H., Okada, M., Nagata, K., Fujimoto, M., Yoshikawa, M., Yamamoto, Y., Shirai, K., Noguchi, R., Ogawa, N., Terui, F., Kikuchi, S., Yamaguchi, T., Oki, Y., Takao, Y., Takeuchi, H., Ono, G., Mimasu, Y., Yoshikawa, K., Takahashi, T., Takei, Y., Fujii, A., Hirose, C., Nakazawa, S., Hosoda, S., Mori, O., Shimada, T., Soldini, S., Iwata, T., Abe, M., Yano, H., Tsukizaki, R., Ozaki, M., Nishiyama, K., Saiki, T., Watanabe, S., Tsuda, Y., 2019. The geomorphology, color, and thermal properties of ryugu: Implications for parent-body processes. Science 364 (6437), http://dx.doi.org/10.1126/science.aaw0422.

Sullivan, R., Thomas, P., Murchie, S., Robinson, M., 2002. Asteroid Geology from Galileo and NEAR Shoemaker Data. Univ. of Arizona, Tucson, pp. 331–350.

Takizawa, S., Katsuragi, H., 2020. Scaling laws for the oblique impact cratering on an inclined granular surface. Icarus 335 (113409), http://dx.doi.org/10.1016/j.icarus.2019.113409.

Thuillet, F., Michel, P., Maurel, C., Ballouz, R.-L., Zhang, Y., Richardson, D.C., Biele, J., Tatsumi, E., Sugita, S., 2018. Numerical modeling of lander interaction with a low-gravity asteroid regolith surface-application to MASCOT on board Hayabusa2. Astron. Astrophys. 615, A41. http://dx.doi.org/10.1051/0004-6361/201832779.

Thuillet, F., Michel, P., Tachibana, S., Ballouz, R.-L., Schwartz, S.R., 2020. Numerical modelling of medium-speed impacts on a granular surface in a low-gravity environment application to Hayabusa2 sampling mechanism. Mon. Not. R. Astron. Soc. 491 (1), 153–177. http://dx.doi.org/10.1093/mnras/stz3010.

Tsuda, Y., Saiki, T., Terui, F., Nakazawa, S., Yoshikawa, M., ichiro Watanabe, S., 2020. Hayabusa2 Mission status: Landing, roving and cratering on asteroid ryugu. Acta Astronaut. 171, 42–54. http://dx.doi.org/10.1016/j.actaastro.2020.02.035.

Tsujido, S., Arakawa, M., Suzuki, A.I., Yasui, M., 2015. Ejecta velocity distribution of impact craters formed on quartz sand: Effect of projectile density on crater scaling law. Icarus 262, 79–92. http://dx.doi.org/10.1016/j.icarus.2015.08.035.

Van wal, S., Çelik, O., Tsuda, Y., Yoshikawa, K., Kawakatsu, Y., 2021. Reduced-gravity experiments of nonspherical rigid-body impact on hard surfaces. Adv. Space Res. 67 (1), 436–476. http://dx.doi.org/10.1016/j.asr.2020.10.018.

Van wal, S., Yoshikawa, K., Tsuda, Y., 2019. Deployment analysis and trajectory reconstruction of minerva-II rovers on asteroid ryugu. In: Advances in the Astronautical Sciences. 168, pp. 1891–1910.

Wada, K., Ishibashi, K., Kimura, H., Arakawa, M., Sawada, H., Ogawa, K., Shirai, K., Honda, R., Iijima, Y., Kadono, T., Sakatani, N., Mimasu, Y., Toda, T., Shimaki, Y., Nakazawa, S., Hayakawa, H., Saiki, T., Takagi, Y., Imamura, H., Okamoto, C., Hayakawa, M., Hirata, N., Yano, H., 2021. Size of particles ejected from an artificial impact crater on asteroid 162173 ryugu. Astron. Astrophys. 647, A43. http://dx.doi.org/10.1051/0004-6361/202039777.

Wada, K., Senshu, H., Matsui, T., 2006. Numerical simulation of impact cratering on granular material. Icarus 180 (2), 528–545. http://dx.doi.org/10.1016/j.icarus.2005.10.002.

Walsh, K., Jawin, E., Ballouz, R.-L., Barnouin, O., Bierhaus, E., Connolly, H., Molaro, J., McCoy, T., Delbo, M., Hartzell, C., et al., 2019. Craters, boulders and regolith of (101955) bennu indicative of an old and dynamic surface. Nat. Geosci. 12 (4), 242–246. http://dx.doi.org/10.1038/s41561-019-0326-6.

Wright, E., Quillen, A.C., South, J., Nelson, R.C., Sánchez, P., Siu, J., Askari, H., Nakajima, M., Schwartz, S.R., 2020. Ricochets on asteroids: Experimental study of low velocity grazing impacts into granular media. Icarus 351 (113963), http://dx.doi.org/10.1016/j.icarus.2020.113963.

Yamamoto, S., Wada, K., Okabe, N., Matsui, T., 2006. Transient crater growth in granular targets: An experimental study of low velocity impacts into glass sphere targets. Icarus 183 (1), 215–224. http://dx.doi.org/10.1016/j.icarus.2006.02.002.

Yano, H., Kubota, T., Miyamoto, H., Okada, T., Scheeres, D., Takagi, Y., Yoshida, K., Abe, M., Abe, S., Fujiwara, a., Hasegawa, S., Hashimoto, T., Ishiguro, M., Kato, M., Kawaguchi, J., Mukai, T., Saito, J., Sasaki, S., Yoshikawa, M., 2005. Touchdown of the hayabusa spacecraft at the muses sea on itokawa. Science 312 (June), 4–7.

Yu, Y., Richardson, D.C., Michel, P., Schwartz, S.R., Ballouz, R.-L., 2014. Numerical predictions of surface effects during the 2029 close approach of asteroid 99942 apophis. Icarus 242, 82–96. http://dx.doi.org/10.1016/j.icarus.2014.07.027.

Zacny, K., Bierhaus, E.B., T. Britt, D., Clark, B., Hartzell, C.M., Gertsch, L., Kulchitsky, A.V., Johnson, J.B., Metzger, P., Reeves, D.M., Sanchez, P., Scheeres, D.J., 2018. Chapter 8 - geotechnical properties of asteroids affecting surface operations, mining, and in situ resource utilization activities. In: Abreu, N. (Ed.), Primitive Meteorites and Asteroids. Elsevier, pp. 439–476. http://dx.doi.org/10.1016/B978-0-12-813325-5.00008-2.